Inhomogeneous probes for Bragg coherent diffraction imaging: Toward the imaging of dynamic and distorted crystals

I. Calvo-Almazán ⬤

Instituto de Nanociencia y Materiales de Aragón (INMA), CSIC - University of Zaragoza, Calle de Pedro Cerbuna 9, 50009 Zaragoza, Spain

V. Chamard ⬤, T. A. Grünewald ⬤, and M. Allain ⬤

Aix Marseille Univ, CNRS, Centrale Med, Institut Fresnel, Marseille, France

This paper proposes an innovative approach to improve Bragg coherent diffraction imaging (BCDI) microscopy applied to time evolving crystals and/or nonhomogeneous crystalline strain fields, identified as two major limitations of BCDI microscopy. Speckle BCDI (spBCDI), introduced here, rests on the ability of a strongly nonuniform illumination to induce a convolution of the three-dimensional (3D) frequency content associated with the finite-size crystal and a kernel acting perpendicularly to the illumination beam. In the framework of Bragg diffraction geometry, this convolution is beneficial as it encodes some 3D information about the sample in a single two-dimensional (2D) measurement, i.e., in the detector plane. With this approach, we demonstrate that we can drastically reduce the sampling frequency along the rocking curve direction and still obtain datasets with enough information to be inverted by a traditional phase retrieval algorithm. Numerical simulations, performed for a highly distorted crystal, show that spBCDI allows a gain in the sampling ratio ranging between 4 and 20 along the rocking curve scan, for a speckle illumination with individual speckle size of 50 nm at the sample position. Furthermore, spBCDI allows working at low intensity levels, leading to an additional gain for the total scanning time. Reductions of a factor of about 40 were numerically observed. Thus, full 3D datasets measured in the 0.2 s time scale at fourth-generation synchrotrons become feasible, with a remarkable potential for the imaging of strongly distorted crystals. Practical details on the implementation of the method are also discussed.

I. INTRODUCTION

BCDI is a 3D microscopy approach based on the numerical processing of a series of diffracted intensities, produced by a 3D finite-size crystalline sample illuminated by a coherent x-ray beam [1–4]. The numerical processing consists in an iterative phase retrieval from the diffracted intensity information, which leads to a 3D complex-valued map of the sample, where the modulus corresponds to the electronic density distribution for a specific family of lattice planes while the phase encodes information about any deviation of these lattice planes from a reference, perfectly periodic crystal [1]. Hence, BCDI is particularly sensitive to crystalline distortions (e.g., strain fields, dislocations, lattice rotations) and is capable of providing 3D images of crystalline samples with sizes ranging from hundreds of nanometers up to a couple of micrometers, with a spatial resolution in the order of a few tens of nanometers [1,2].

The use of hard x rays (with energies larger than 8 keV) eases the implementation of BCDI for *in situ* experiments, with exciting applications in a wide variety of scientific fields including energy-related materials (e.g., catalysis, batteries [5–7]), environment (e.g., mineral dissolution [8,9]), or biomineralisation [10], only to cite a few. However, BCDI fails at imaging particles with strongly nonhomogeneous crystalline strain fields, limiting its scope to crystals with rather narrow strain distributions [11,12]. Additionally, the data acquisition process involves the collection of a series of 2D diffraction patterns with a planar detector, along the rocking curve (RC) direction. It corresponds to the sampling of the 3D Bragg peak intensity distribution, performed with an angular scan of the sample about the axis perpendicular to the diffraction plane [13] and at a sampling frequency of at least twice the Nyquist frequency along this direction [14,15]. This time-consuming data acquisition process affects directly the temporal resolution of 3D BCDI, which is rather poor as the sample must remain static during the time needed to fully explore the 3D intensity distribution of the crystal [16]. This limitation precludes the imaging of dynamic systems, especially for highly distorted crystals, which require a very high degree of oversampling, i.e., increasing the number of measurements along the RC scan [17]. In this paper, we propose an approach, called *speckle* BCDI (spBCDI), which introduces additional information in the dataset without increasing the acquisition time.

Following the progress in optical microscopy [18–21] and inspired by several implementations in the x-ray regime [22–26], we propose to manipulate the coherent x-ray *incident* wavefront with a *modulator phase plate* (MPP) to

perform BCDI with a speckled, strongly nonuniform beam. In reciprocal space, the intensity distribution produced by a 3D crystalline sample under a plane-wave illumination is described as the square modulus of the diffracted field, itself given by the 3D Fourier transform (FT) of the sample, for measurements performed in the Fraunhofer regime [1,2]. Under nonuniform illumination, the scattering process induces a 3D convolution of the sample FT by a structured kernel acting along the direction perpendicular to the incident beam [19,27]. In the framework of the Bragg diffraction geometry, because the direction of the incoming beam does not align with the exit direction, any diffracted intensity is expected to probe the sample FT *concurrently* at various positions along the RC direction. Thereby, the high structural richness of the speckle illumination can be used in BCDI to increase the 3D information content of each detector slice in the RC direction, thus reducing the sampling frequency, and hence, the measurement time.

Herein, numerical simulations show this effect, which improves for larger incident angles and smaller speckle sizes. It enables, not only to relax the sampling conditions in a RC scan down to factors ranging 4–20, but also to reduce the signal-to-noise ratio that is required for a successful reconstruction. Thereby, it yields potential reductions of the measurement time up to a factor of about 40 with respect to plane-wave BCDI methodology, which translates into total acquisition times of the order of 0.2 s for the whole dataset, at fourth-generation synchrotron sources [28–30]. Another important advantage of spBCDI, is the observed robustness of the method with respect to heavily distorted crystals, which allows one to image crystalline samples with phase distributions containing abrupt discontinuities between domains and/or large strain fields.

Finally, we note that this mechanism by which speckle illuminations allow a sparser sampling in the RC direction arises only if the exit direction does not align with the incoming direction of the beam, i.e., it is specific to the Bragg geometry. In the (more standard) forward scattering geometry, the exit and incoming directions align and speckle illuminations are mostly expected to increase the transverse resolution of 2D reconstructions, see for instance [24,25,31–33]. To the best of our knowledge, speckle-based illumination CDI methods have never been proposed and tested in the Bragg scattering geometry.

This article is structured in three main sections. Section II introduces the sort of structural information encoded in reciprocal space when the crystal is illuminated by a plane wave or a speckled beam and its consequences for the sampling conditions. It further provides a qualitative guide to estimate the reduction factor for the sampling along the rocking curve, which is found to be a function of the speckle size and the incident angle. Section III numerically addresses the performances of spBCDI regarding several experimental parameters, including various degrees of sampling, signal-to-noise ratio, knowledge of the exact crystal shape and the incident angle. Comparison of the method with respect to standard BCDI is also presented, evidencing dramatic gains in acquisition time and therefore justifying development at fourth-generation synchrotron

sources, whose practical implementation is briefly discussed in Sec. IV.

II. INFORMATION ENCODING VIA NONUNIFORM ILLUMINATIONS

BCDI is a 3D lensless microscopy approach aiming to solve the *phase problem*, i.e., retrieve the phase of a complex-valued field, from the measurement of its intensity. It requires the fine sampling (or oversampling) of the 3D diffracted intensity produced by a nano- or micro-sized crystal illuminated with a plane wave [34,35] (see Fig. 1). In theory, the illuminating plane wave can be produced by a pinhole in the far-field of the crystal but, in practice the pinhole is replaced by a focusing optics, which produces an illumination profile much larger than the crystal size. In the perpendicular direction to k_f, the oversampling is ensured by the 2D-detector pixel size, whose angular resolution can be incremented by increasing the sample-to-detector distance [1], a question, which is not further addressed in this paper. To probe the third direction, an angular scan is usually performed [13]. It consists in the acquisition of a series of diffraction patterns measured while the crystal is illuminated at different orientations, such that the detector plane records the intensity distribution around a specific point of the periodically structured reciprocal space, i.e., a Bragg peak [see Figs. 1(b) and 1(c)]. The angular scan often corresponds to the rocking curve scan, so that the crystal is tilted about an axis perpendicular to the diffraction plane [Fig. 1(c)] [13,36]. However, other 3D reciprocal space sampling schemes can be designed, introducing different angular or energy scans [3,13,27,36]. Although we did not explore other scanning modalities further, a similar idea can be applied at a fixed angular position, as spBCDI generates 3D information in the 2D plane of the detector, owing to the significant tilt between the Fourier transform of the illumination (perpendicular to the incoming beam direction) and the detector plane.

The oversampling ratio (OSR) σ is linked to the sampling step δ_q via the relation:

$$\sigma \equiv \frac{1}{\delta_q \Delta_r} \tag{1}$$

where Δ_r is the object size in the conjugated direction of reciprocal space (typically, the spatial extension of the investigated sample is ∼1 μm in any dimension). In n-D phase retrieval, with $n > 1$, if the support is known, the Shannon-Nyquist theorem establishes that $\sigma \geqslant 2$ for all the three dimensions of reciprocal space is sufficient [37], to ensure a unique solution up to trivial, irrelevant ambiguities [38]. Equation (1) enables to define an OSR along the RC direction $\widetilde{k}_3$, σ_{RC}, which will depend on the sampling step δ_q determining the distance between contiguous detector slices in a RC scan [see Fig. 1(c)]. It can be connected to specific experimental parameters since $\delta_q = |\mathbf{G}_{HKL}|\delta\theta$, where $\delta\theta$ is the angular step by which the sample is tilted for each acquisition along the RC scan and where $\mathbf{G}_{HKL}$ is the Bragg vector associated to the *HKL* planes family in the reciprocal space. Thus, complying with the Shannon-Nyquist criterion along the RC imposes that $\sigma_{RC} \geqslant 2$, which leads to the adjustment of the angular step with respect to the object size. In practice,
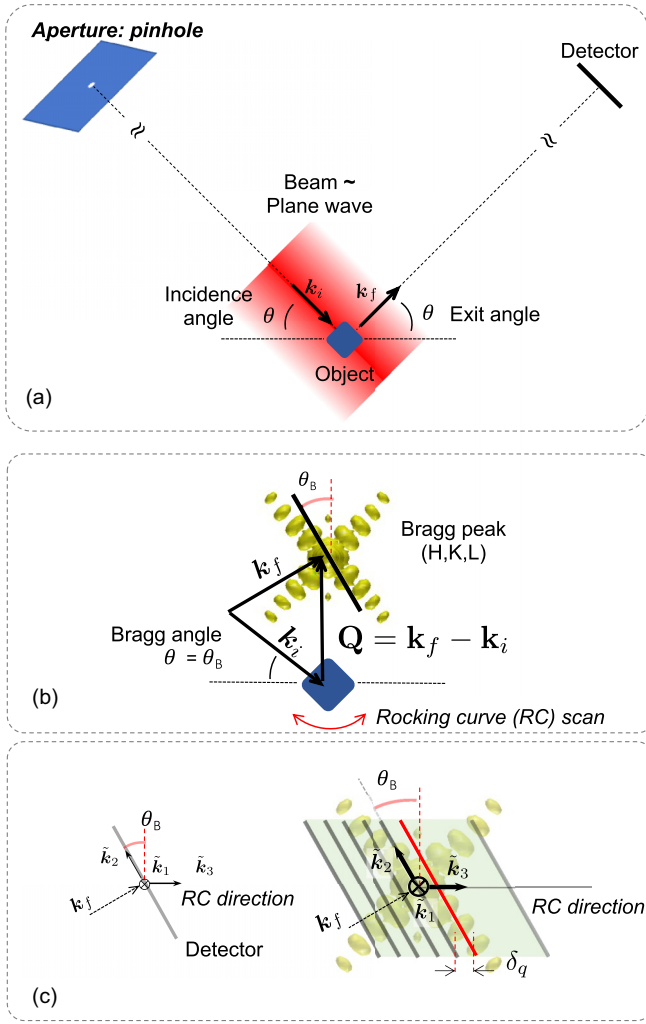
FIG. 1. Bragg coherent diffraction imaging (BCDI). Illumination and geometrical considerations. (a) A typical x-ray Bragg coherent diffraction imaging experiment can be described as a crystalline sample illuminated by a plane wave generated by a point-wise source (i.e., a pinhole) in the aperture plane, which is located in the far-field of the sample. (b) The incident vector $\mathbf{k}_i$ and the exit vector $\mathbf{k}_f$ normal to the detector surface are in "Bragg condition", when the momentum transfer vector $\boldsymbol{Q} := \boldsymbol{k}_f - \boldsymbol{k}_i$ coincides with a point in the reciprocal lattice, hence defining a Bragg angle θ_B. In that geometry the detector records a 2D slice of the diffracted intensity distributed around the Bragg peak. (c) During the RC scan, the rotation of the reciprocal lattice about its origin is equivalent to the sampling of the intensity produced by the 3D Fourier transform of the sample along the RC direction $\tilde{\mathbf{k}}_3$. Because the RC direction is nonorthogonal to the detector surface, the measurement is naturally described within a nonorthogonal frame $(\tilde{\boldsymbol{k}}_1, \tilde{\boldsymbol{k}}_2, \tilde{\boldsymbol{k}}_3)$.

one gets $\delta\theta \ll 1°$, hence, many (typically tens of) rocking steps δ_q are required to fully sample the diffracted intensity [1,2,6]. Such a stringent condition is a direct consequence of the way a plane wave extracts the structural information about the sample. More specifically, let us assume the usual Born approximation within the scalar diffraction theory [39]. In this case, the 3D spatial distribution of diffracting sources is given by $\psi = P \times \rho$, with ρ the complex-valued sample and P the illumination at the sample position [26,40,41]. The diffracted

field at the detector plane, located in the far-field, is a "slice" of the following 3D quantity [42]:

$$
\begin{aligned}
\Psi &:= \mathcal{F}\psi \\
&= (\mathcal{F}P) \otimes (\mathcal{F}\rho)
\end{aligned}
\tag{2}
$$

where $\otimes$ denotes the 3D convolution operator and $\mathcal{F}$ is the 3D FT operator. In the x-ray regime, the illumination P is mostly an invariant function along the incoming direction of the beam $\boldsymbol{k}_i$ [43]; this is a direct consequence of the poor numerical apertures (NA $\sim 10^{-3}$) available for x rays [44]. In standard BCDI, this illumination is just a plane wave (i.e., $\mathcal{F}P$ is a centered Dirac distribution) and we deduce from Eq. (2) that the diffracted intensities in the BCDI dataset are actually drawn from the 3D intensity of the FT of ρ itself. Therefore, the sampling conditions for the BCDI experiment are exclusively determined by the sample size. When the illumination P is spatially inhomogeneous (e.g., with the introduction of a random phase-mask at the aperture plane) the associated convolution kernel $\mathcal{F}P$ spreads $\mathcal{F}\rho$ along a direction in reciprocal space that is perpendicular to the incident beam. In this situation, a single slice in Eq. (2) actually samples $\mathcal{F}\rho$ *concurrently* at various positions along the rocking curve scan. The above reasoning suggests that the illumination modifies the range of information, which is accessible from a single detector slice, and thus, may relax the oversampling requirements. In Fig. 2, we illustrate this idea, with three specific configurations corresponding to three standard microscopy modalities that we discuss in the next paragraph. Note that in the three cases, the aperture is in the far field of the sample. Furthermore, as we are measuring with hard x rays, we assume to be in the weak scattering regime, which justifies the simple links between the properties of the aperture, the size of the illumination in the focal plane and the spreading of the signal in the Fourier space. To complete the description, the difference between the forward geometry case and the Bragg geometry case is discussed in the Supplemental Material (SM) [46], evidencing the dependence of our approach with the momentum transfer value.

(i) The first configuration corresponds to the *focused beam* illumination shown in panels (a) and (a′) in Fig. 2. It is the foundation of ptychography in CDI [40,45,47,48]. As the size of the illumination at the focal plane is governed by the numerical aperture of the focusing optics, the curved wavefront at the focusing position is not shown. This results in an illumination where most of the energy is localized in a central lobe of transversal width Δ^{foc}. In reciprocal space, this leads to a frequency mixing spanning a window with a transversal extension of $\Delta \propto 1/\Delta^{foc}$. Along the RC direction, a single detector slice is then sensitive to the structural information within the domain $\sim\Delta \sin\theta_B$, as θ_B coincides with the incidence angle for a symmetric reflection. Such an increase in sampling efficiency of the reciprocal space is obviously counterbalanced by the inability to extract this information over a large spatial field-of-view (FOV), because of the limited size of the focused probe onto the sample. A method providing a large FOV with relaxed sampling conditions in reciprocal space is thus, desirable.

(ii) The second configuration, shown in panels (b) and (b′), borrows its principle from *structured illumination microscopy* (SIM), a super-resolution method developed in fluorescent
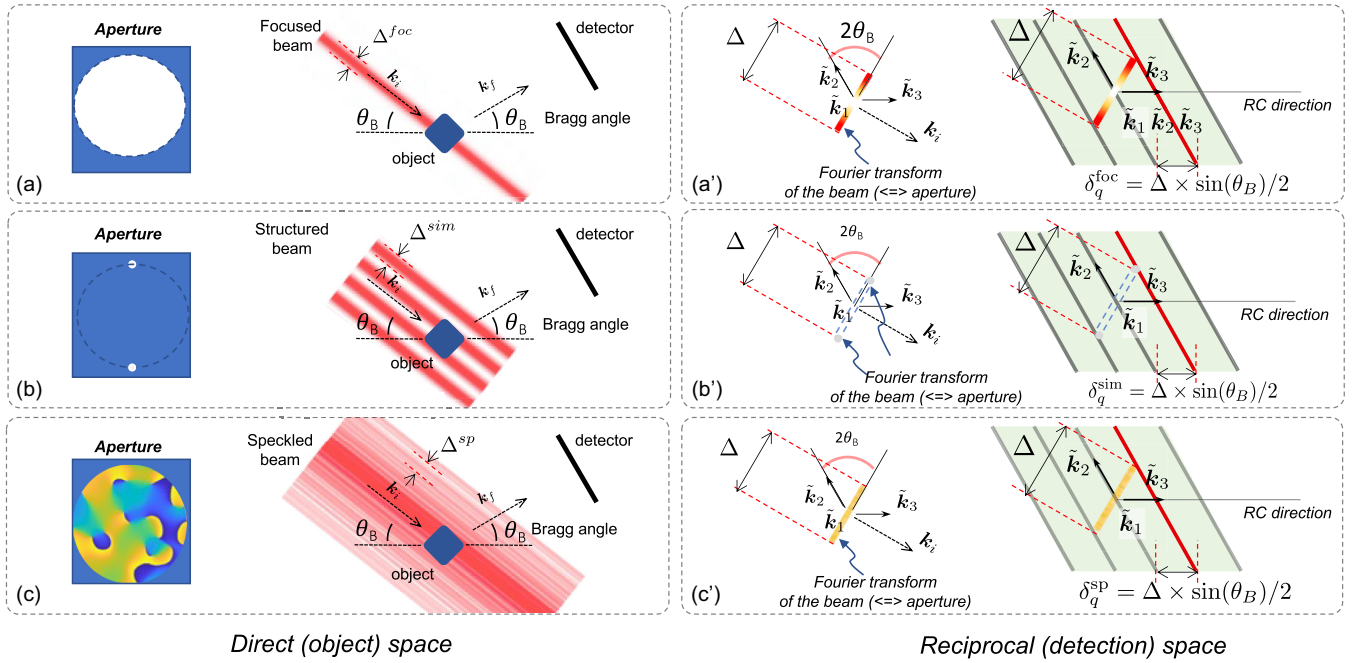
FIG. 2. Schematics of microscopy modalities using inhomogeneous probes. (a) A focused beam (for simplicity, the curved wavefront is not shown as only the lens aperture governs the size of the focal spot), (b) an harmonic structured illumination, and (c) a speckled beam. Each inhomogeneous probe is characterized by its complex transmission function within the optical aperture. The numerical aperture sets an identical bandwidth Δ for each kernel $\mathcal{F}P$ spreading $\mathcal{F}\rho$ in reciprocal space. Note that the aperture and the detector always located at the far-field of the sample.

(incoherent) microscopy in the early 2000's [20]. To the best of our knowledge, SIM has never been adapted to BCDI. Yet, the simplicity of the mechanism at work to extract frequency information otherwise inaccessible with an uniform illumination makes it particularly appealing [20,21,49]. In SIM, a pair of coherent sources located in the aperture plane of the lens generates an harmonic illumination that is invariant along the beam direction [see Fig. 2(b)] resulting in a highly inhomogeneous illumination over a large FOV in the transverse plane. Let us assume that the FT of P is a pair of Dirac distributions located in $\pm\bar{q}$ with $\bar{q}$ a momentum transfer vector perpendicular to the incoming wavevector k_i and such that $2|\bar{q}| = \Delta = 1/\Delta^{\text{sim}}$, where Δ^{sim} is the spatial period of the illumination [see Fig. 2(b′)]. The diffracted wave field, given by Eq. (2), is then a pair of shifted copies of the original Bragg peak,

$$\Psi_{\text{SIM}}(\boldsymbol{q}) = (\mathcal{F}\rho)(\boldsymbol{q} - \bar{\boldsymbol{q}}) + (\mathcal{F}\rho)(\boldsymbol{q} + \bar{\boldsymbol{q}}). \qquad (3)$$

The relation above indicates that the detector centered at the Bragg peak provides simultaneously the information that would be obtained from two successive measurements with a plane wave, shifting the peak along $\widetilde{\boldsymbol{k}}_3$ by $|\bar{\boldsymbol{q}}|\sin\theta_B$ and $-|\bar{\boldsymbol{q}}|\sin\theta_B$, respectively; in other words, a *multiplexed* sampling of the Bragg peak is performed.

This capacity to extract an information content otherwise inaccessible with an uniform illumination is at the very core of SIM in fluorescence microscopy [20,21]. This elegant and simple strategy has nevertheless two limitations. The first one relates to the use of (extremely small) pinholes to generate the pair of coherent x-ray sources at the aperture plane. This implies a vast loss of flux at the sample position, which is

highly detrimental to the counting statistic of the dataset. The second limitation relates to the intensity of the harmonic pattern that vanishes periodically in the transverse plane. Clearly, because the sample information cannot be retrieved at regions that have not received any photons, additional measurements with shifted positions of the illumination pattern are required, to probe all parts of the sample. This issue is not specific to harmonic patterns as fully coherent, strongly inhomogeneous illuminations are probably difficult to achieve practically, without observing intensity holes in some places.

(iii) The third configuration, depicted in panels (c) and (c′) of Fig. 2 consists in speckle illumination at the sample position, generated by a random phase mask located in the aperture plane. It allows maximizing the photon flux at the sample position while still ensuring an efficient mixing of the information in the reciprocal space. We discuss below the design of such illuminations and their properties in the framework of BCDI acquisitions.

A. Speckle beam for BCDI acquisitions

At hard x-ray energies, the incoming beam wavefront can be manipulated by combining a phase plate, called modulator phase plate (MPP) with a focusing optical device (i.e., a lens). Such a combination produces a strongly nonuniform illumination, called *speckle illumination*, at the focal plane of the lens, where the sample is located. Because of the limited numerical aperture of the lens, the speckle pattern can be considered as self-similar along a few tens of micrometres in the vicinity of the focal plane. A sketch for the simulation of such a speckled probe and an illustration of its behavior
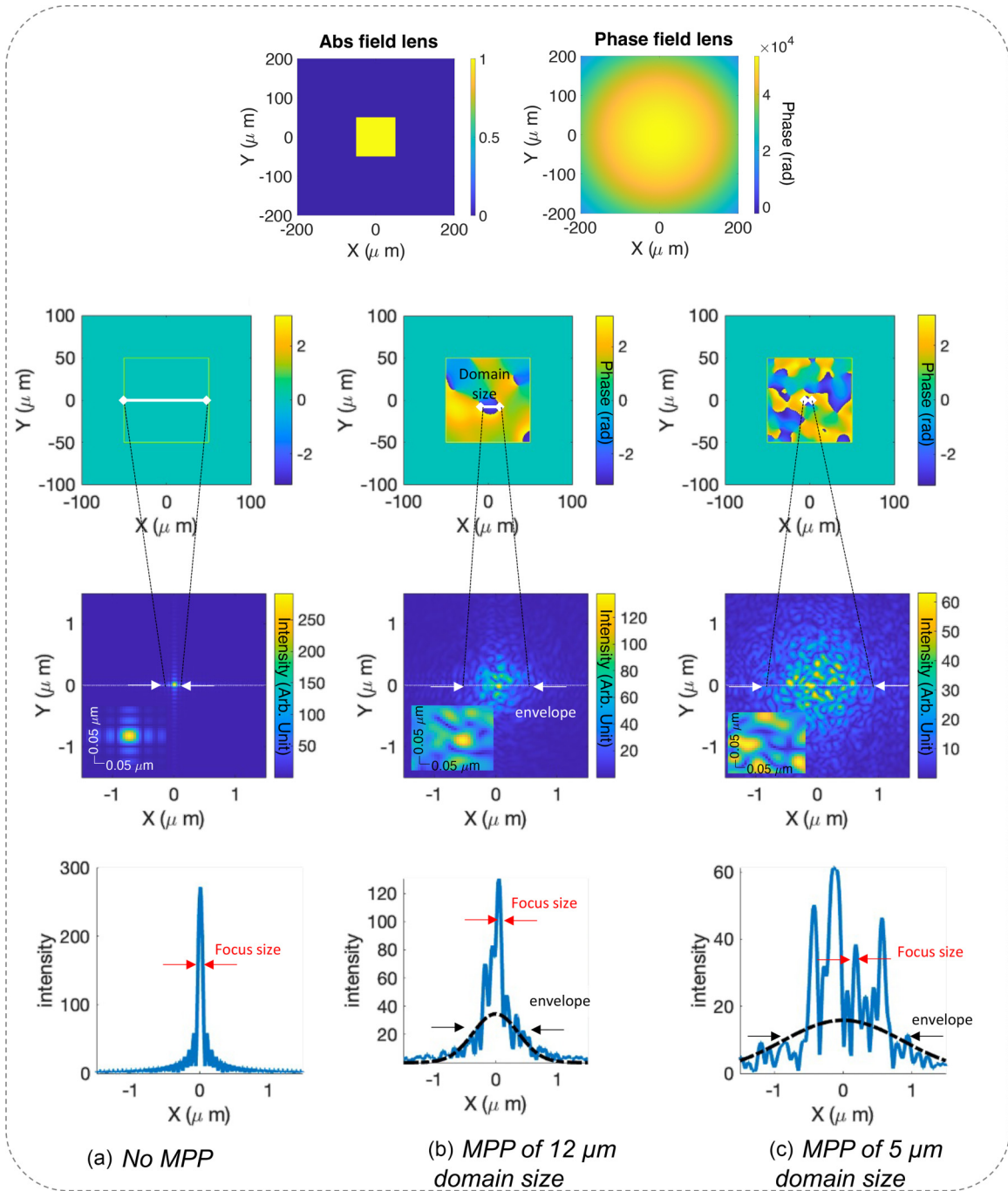
FIG. 3. Speckle beams achieved with the combination of a focusing lens producing a focal spot of 50 nm and two modulator phase plates (MPP) of different domain sizes: 5 and 12 μm. The first row represents the lens complex transfer function (the amplitude in the left and the parabolic phase in the right side). The second row shows the phase configuration of each MPP. Note that the focusing lens and the MPP form an ensemble, which is located in the far-field of the sample, and which produces the illuminations shown in the third row. The insets are a zoom into the central part and provide a measure of the speckle size. Finally, the last row shows a 1D cut through the horizontal direction of the illumination. More details can be found within the SM [46].

in the vicinity of the focal plane are shown in the SM [46]. The MPP consists of a uniform optical aperture where phase-shifting domains are randomly distributed. When a coherent x-ray beam illuminates the MPP, the phase of its wavefront is strongly perturbed. The focusing of such a beam with an optical device like diffractive lenses (e.g., Fresnel zone plate [50] or multilayer-Laue lenses [51]) or refractive/reflective

lenses (e.g., compound refractive lenses [52] or KB mirrors [53]), produces intense interferences at the focal plane resulting in a *speckled illumination* (see Sec. 2 within the SM for more details [46]). As shown in Fig. 3 , the features of the speckled illumination are fully controlled by the MPP and by the lens. In particular, the speckle size is determined by the lens aperture; it is then identical to the lateral extension of

the focal spot that would be obtained with the focusing optics alone. The FOV of the speckled beam (i.e., the FWHM of the illumination envelope) is governed by the correlation-length of the random phase domains in the MPP; it is then directly related to the size of the phase domains in the modulator (see Fig. 3).

Similar to SIM, the intensity of the generated speckle field is going to vanish in some lateral positions. To minimize the impact of these dark regions, a few RCs with the speckle illumination shifted laterally are needed to retrieve a robust estimate of the sample structure. However, the isotropic nature of the correlation of the speckle provides more flexibility than the harmonic pattern to achieve a nonzero total photon deposit. Standard piezoelectric translation stages commonly used in several synchrotron beamlines can routinely achieve spatial shifts comparable to the speckle size (e.g., ∼20–200 nm) [48,54].

Hence, using a random phase MPP to manipulate the x-ray wavefront is therefore a suitable strategy for structured illumination experiments, for its ability to generate a speckle illumination over a large FOV and with almost no loss of coherent flux (besides the absorption by the material of the phase modulator). Moreover, similar to the harmonic illumination or the focused beam, the speckled beam also performs the "frequency-mixing" action, which is expected to foster the sampling efficiency along the RC direction [Fig. 2(c')]. In the next section, we derive the relaxed sampling conditions along the RC that can be achieved with specific speckle beam parameters.

B. Relaxed sampling condition along the RC

Speckle-BCDI exploits the multiplication of shifted copies of the object FT arising from a nonuniform illumination to increase the amount of 3D information in each 2D slice of the RC scan [see Eq. (3) and Fig. 2]. In the weak-scattering regime, the (known) illuminating field is unsensitive to the sample and can be used as a reference. This effect is predicated on the structural information distribution in reciprocal space resulting from the convolution between the illumination and the object FTs. Thus, the FT of the illumination determines the extent of the reciprocal space that a single detector slice is capable to probe. This sets a lower limit for the reciprocal space step along the RC direction δ_q^{sp}, which directly leads to the minimum angular sampling step along the RC scan. This reasoning in reciprocal space is actually equivalent to a reasoning in direct space, performed on a single speckle grain. In particular, we consider the footprint of the speckle grain Δ_r^{sp} expressed as follows:

$$\Delta_r^{sp} = \frac{\Delta^{sp}}{\sin \theta_B} \tag{4}$$

where Δ^{sp} is the lateral extension of the speckle grain (see Fig. 4). It results that

$$\delta_q^{sp} = \left(2\Delta_r^{sp}\right)^{-1} = \frac{\sin \theta_B}{2\Delta^{sp}} = \frac{\Delta \sin(\theta_B)}{2}. \tag{5}$$

TABLE I. Illustration of the gain in sampling induced by the use of a speckle beam compared to the plane-wave illumination at the Shannon-Nyquist criterion ($\sigma_{RC} = 2$), for different incident angles and different beam speckle sizes. The sample is a cube of edge $L = 700$ nm and diagonal $\Delta_r = 990$ nm. A symmetrical reflection is considered so that the incident angle is equal to the Bragg angle.

Δ^{sp}	[nm]	50		80		100	
θ_B	[degree]	9	45	9	45	9	45
σ_{RC}^{min}		0.64	0.14	1.0	0.23	1.29	0.29
Gain wrt $\sigma_{RC} = 2$		3.1	14	1.9	8.8	1.5	7

Substituting Eq. (5) in Eq. (1), yields an estimate of the minimum sampling ratio σ_{RC}^{min},

$$\sigma_{RC}^{min} = \frac{1}{\delta_q^{sp}\Delta_r} = \frac{2\Delta^{sp}}{\Delta_r \sin \theta_B} \tag{6}$$

defining a lower bound for the sampling ratio along the RC scan, for which the inversion of the intensity data is still expected to be unique. This rule is illustrated in Fig. 4, which also displays the impact of the incidence angle in the separation between two successive detector slices. The interest of this approach is further underlined by considering the following experimental example, where a cubic sample of edge $L = 700$ nm and diagonal $\Delta_r = 990$ nm is illuminated at two different incident angles, 9° and 45°, by three different focused beams, characterized by their speckle sizes: 50, 80, and 100 nm. Table I summarizes the resulting σ_{RC}^{min} values, which are further compared to the case $\sigma_{RC} = 2$, the usual sampling condition for the plane-wave BCDI approach. Important gains in sampling efficiency, of about one order of magnitude, can be expected at larger incidence angles and smaller speckle sizes. A refined estimation of the accessible gains will be further provided with the numerical experiments summarized in the next section.

III. NUMERICAL DEMONSTRATION OF spBCDI

Figure 5 illustrates the principle of spBCDI on a perfect cubic crystal. While in standard BCDI, the diffraction of a plane wave by a cubic crystal produces in the far field Bragg peaks decorated with fringes of width $2\pi/\Delta_r$ and perpendicular to its facets [see Fig. 1(b)], in spBCDI, the resulting diffracted field is the convolution between the FT of the speckle illumination and the FT of the object [see Eq. (2)]. The diffracted 3D intensity results in a series of copies of the Bragg peak shifted (and weighted) continuously in the plane transversal to the beam propagation. This process replicates the information carried by the FT of the object along a direction, which aligns partially with the RC direction. In this section dedicated to the numerical demonstration of spBCDI, we first describe the design of the numerical model including a 3D complex-valued sample and a highly structured speckle beam. Results and performances of the developed iterative inversion scheme are presented next.
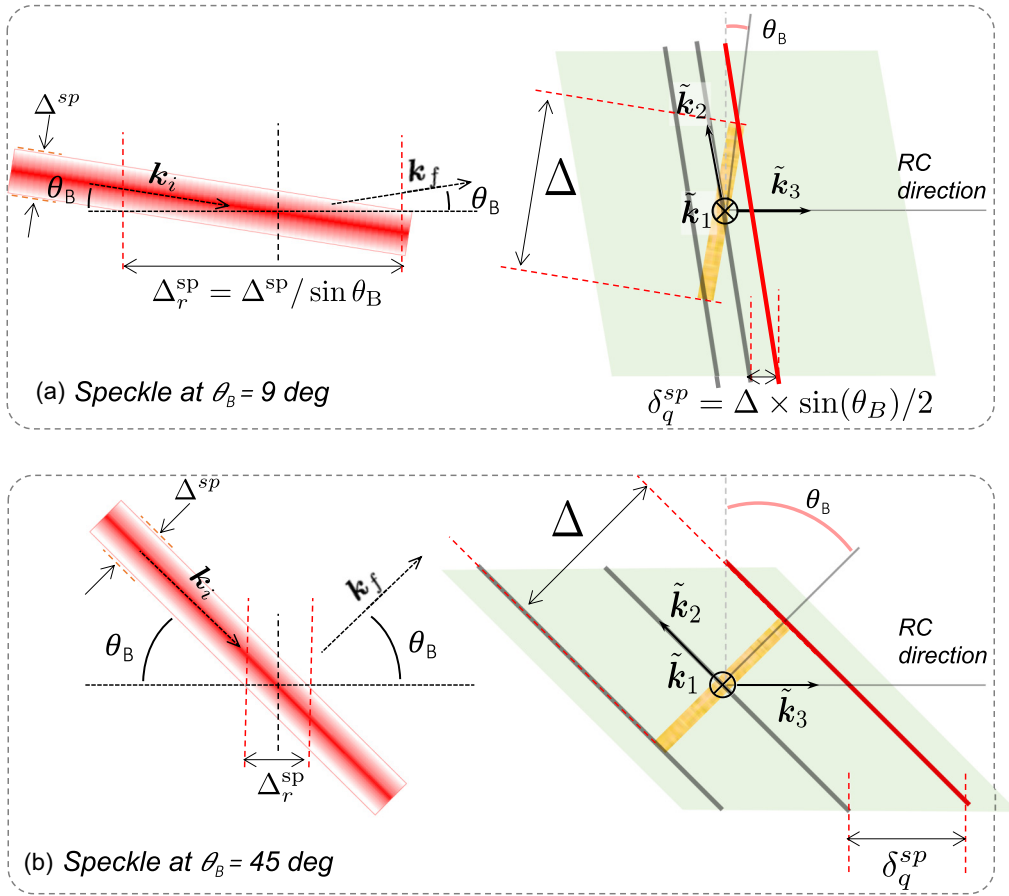
FIG. 4. Effect of the incident angle on the OSR sampling of reciprocal space. (a) The shallow angle case ($\theta_B = 9°$). (b) The large angle case ($\theta_B = 45°$). The left part of the panels depicts the speckle footprint along the rocking curve direction, while the right part of the panel describes how the numerical aperture bandwidth acts in the reciprocal space.

A. Speckle-BCDI simulated measurements

The numerical experiments highlight the relevance of sp-BCDI for efficiently imaging 3D crystalline samples. We anticipate that this method yields different performances as a function of a large set of parameters, such as the sampling rate along the RC, the accessible intensity dynamical range, the incidence angle, the crystalline strain complexity, the a priori knowledge of the sample shape, the speckle distribution, to cite only a few. In this paper, we focus our investigations on a selection of them: the RC sampling rate, the signal-to-noise (SNR) ratio, the sample support, and the incidence angle. The effect of the other parameters will be discussed in the last section.

Our numerical tests involve a highly distorted crystal, produced from the cubic particle depicted in Fig. 5, multiplied by a complex-valued field $\exp i\phi(\mathbf{r})$. In BCDI, this phase $\phi(\mathbf{r})$ is mathematically described by $\phi(\mathbf{r}) = \mathbf{G}_{HKL} \cdot \mathbf{u}(\mathbf{r})$, $\mathbf{u}(\mathbf{r})$ being the atomic displacement vector arising from the internal distortion of the crystalline lattice [1,2,55]. For further comparison with previously published papers, the strain and its distribution are further described in the Sec. 5 within the SM [46] (and in the references therein [56–58]). Given the real-space sample size and the phase distribution, the nonhomogeneous part of the strain is obtained assuming that $\mathbf{G}_{HKL}$ is the (104) Bragg reflection of calcite [9,59]. The

strain, a unitless quantity, corresponds to the ratio of the lattice mismatch (between distorted and reference crystal) to the lattice parameter of the reference crystal. In the presented case, the reference lattice parameter value is chosen equal to the mean value of the distorted lattice parameter (only the inhomogeneous part of the strain is discussed as this is the critical parameter in BCDI). As shown in the SM (Fig. 7 in [46]), the strain extends over one order of magnitude: a large part of the strain is in the order of a few 10^{-4} with, however, a significant amount of the strain increasing up to a few $\pm 4 \times 10^{-3}$, spanning a total nonhomogeneous strain distribution of almost 10^{-2}. The relevance of the strain field in comparison with experimental studies is discussed in the last section of the paper.

A 3D image of the system with cuts of its modulus and phase through the main orthogonal planes (i.e., XY, XZ, YZ) is represented in Fig. 6. Hereafter, the simulation parameters for the speckle illumination and the scattering geometry are summarized; an equivalent summary can be found in the SM [46].

Firstly, the speckle illumination is simulated considering a focus size of 50 nm and a MPP producing an envelope of FWHM ~2 μm, which fully illuminates the cubic crystal of 700 nm edge [see Fig. 3(b)]. Along the beam propagation direction, the speckle pattern is self-similar and the
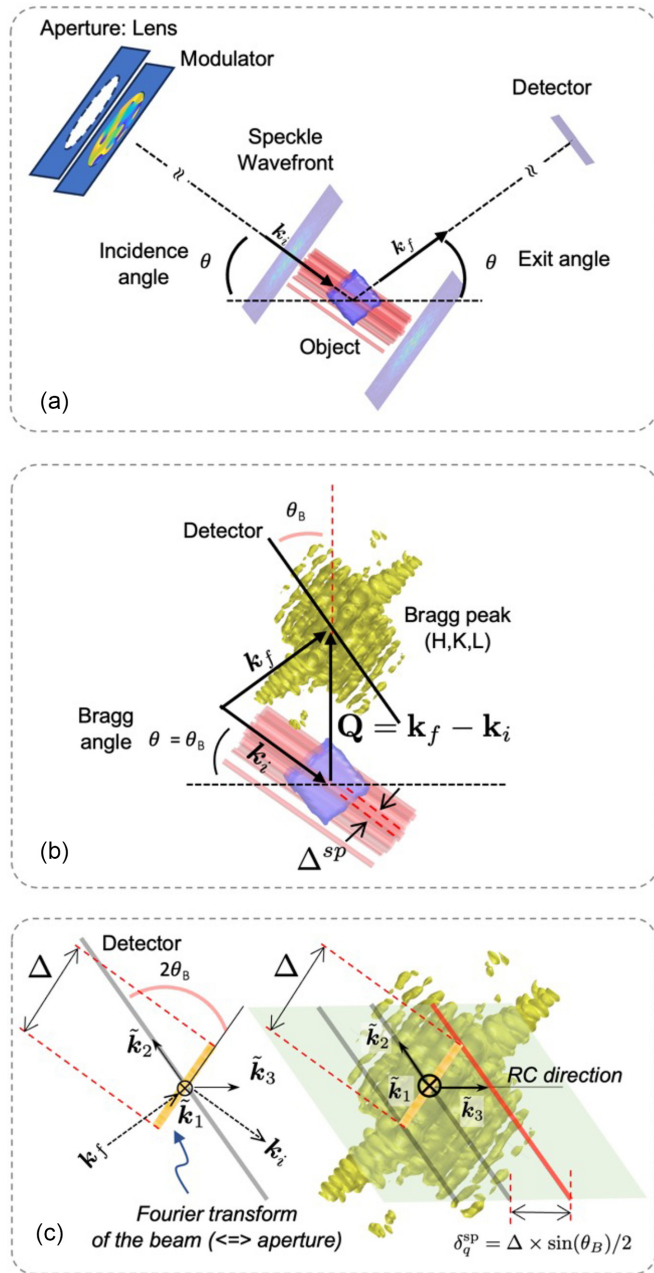
FIG. 5. (a) Schematics for the spBCDI set-up. The lens and the modulator phase plate (MPP) are in the same plane; the sample is located at the far-field of the lens and MPP plane; the detector is placed in the far-field of the sample. Therefore, the connection between the lens/MPP and the sample planes is a Fourier transform. Likewise, the connection between the sample and the detector planes is another Fourier transform. (b) Illustration of the position of the detector in reciprocal space when the incidence angle is adjusted to a Bragg angle. It records a 2D cut of the diffracted intensity distribution around the (*HKL*) Bragg peak. (c) Relation between the sampling step and the resulting set of 2D cuts across the diffracted intensity (on the right) and the Fourier transform of the lens/MPP ensemble, Delta (on the left).

depth of focus, given by λ/NA^2, is about 77 µm (see the SM [46]).

Regarding the scattering geometry, two extreme incident angles are chosen: (i) a shallow angle of 9° and (ii) a larger

angle of 45°. The shallow angle case has been chosen to reproduce a realistic reflection, i.e., the (104) calcite reflection at 13 keV. For this incident angle, a numerical window of 64 × 64 × 90 pixels (with isotropic pixel sizes of 30 nm) has been chosen such that the cube of $\sim 20^3$ total pixel span fits at least three times in each direction (the pixels outside of the object support have been set to zero). This ensures that the autocorrelation function of ρ is fully contained in the simulation array, and hence, prevents cycling aliasing [34]. Equivalently, it guarantees that the diffracted intensity is oversampled with sufficient rates of $\sigma_x = 3.2$, $\sigma_y = 3.2$ (in the detector plane) and $\sigma_{RC} = 4$ (along the RC).

The wider angle case serves to explore the regime where σ_{RC} is drastically diminished. However, for values of $\sigma_{RC} \ll 1$, the quality of the reconstruction can be limited by the reduced number of diffraction patterns (the initial numerical window at $\sigma_{RC} = 4$ contains only 90 pixels in the RC direction). To avoid this potential limitation, the numerical window has been enlarged by adding several diffraction patterns (DP) in the RC direction, but, without changing the sampling step δ_q. Thereby, the extension of the numerical window in real space is preserved, but the physical pixel size is reduced along the direction conjugated to the RC direction. In practice, the new grid contains 64 × 64 × 396 pixels of size 30 nm × 30 nm × 10 nm size. To preserve the 3D phase map in this new scattering geometry, the original object in Fig. 6 is interpolated onto the new grid.

The above described sample, beam, and scattering geometries determine the distribution of the oversampled 3D intensity dataset, which is given by the square modulus of the scattering volume FT, defined as the 3D product of the beam and sample. To test the ability of the phase-retrieval algorithm to reconstruct under-sampled spBCDI data (i.e., data acquired with larger angular steps) we build a set of 3D binary masks discarding, in the original oversampled 3D intensities, the appropriate number of slices along the RC direction. Each 3D mask corresponds to a specific sampling condition along the RC direction and is used within the reconstruction algorithm to select the series of planes to invert at a particular sampling condition. Thereby, the undersampled datasets are produced in a new grid, which is directly a sub-ensemble of the original grid. It prevents the direct manipulation of the crystal and provides a flexible way to simulate various sampling ratios σ_{RC}. In our simulation, σ_{RC} varies from 4 down to 0.06. Hence a ratio of 4 corresponds to the complete dataset, while a ratio of 2 corresponds to sampling at the Shannon-Nyquist frequency and a ratio of 0.5 corresponds to using 1 over 8 diffraction patterns along the RC direction. Moreover, to avoid zones without photon deposition in the sample volume, the speckle illumination needs to be shifted. Therefore, each spBCDI dataset consists of a series of four RC scans at shifted positions of the beam and, thus, increasing proportionally the number of diffraction patterns.

For this study, different intensity levels have been chosen, to push the test to the limits of the method in the context of high rate measurements. To reproduce realistic intensity levels, the signal intensity has been chosen according to a range of SNR values, between 2000 down to 35 ph/pixel, corresponding to the maximum of intensity in the 3D diffraction pattern (before the binary mask is applied). For this, each
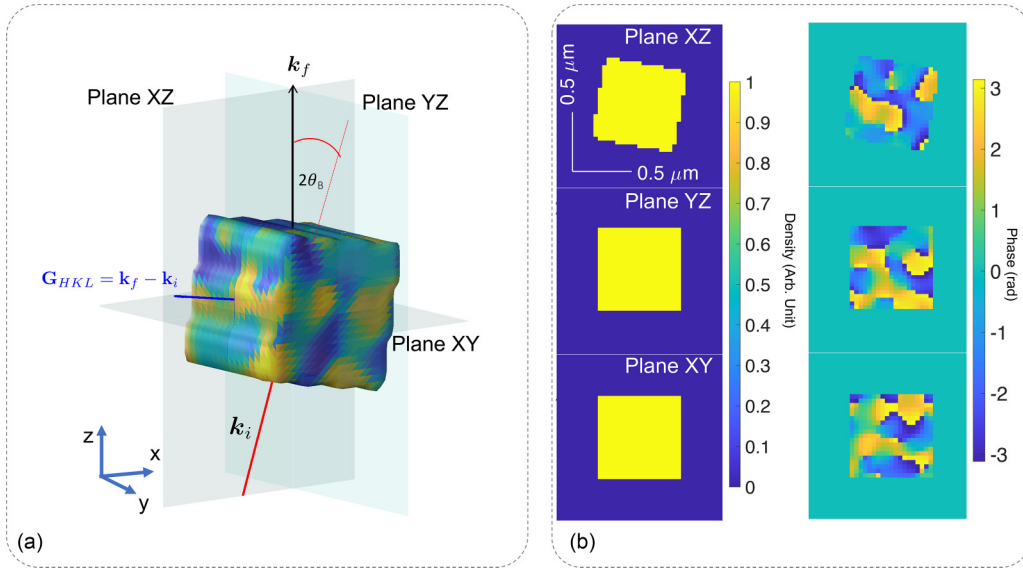
FIG. 6. (a) 3D representation of the nonhomogeneously strained crystalline cube, in the scattering geometry corresponding to an incident angle of 9°. The color map encodes the phase at the surface. The vectors represent the incident $\boldsymbol{k}_i$ and exit $\boldsymbol{k}_f$ beams and $\mathbf{G}_{HKL}$ is the Bragg vector, which coincides with the momentum transfer $\boldsymbol{k}_f - \boldsymbol{k}_i$. (b) Cuts through different planes of the modulus (left) and the phase (right) of the cubic crystal.

RC scan is normalized by the total number of photons deposited in the three dimensions (i.e., a division of the 3D data matrix containing one RC scan by the sum in all directions of the diffracted intensities). Afterwards, the normalized data are multiplied by a factor to reach the specific SNR levels. Poisson noise is eventually added to the intensity obtained in the diffraction planes to simulate all stochastic fluctuations in the photon count rate, either they arise from the illumination or from the detection. This provides a convenient way of characterizing the noise level and it is applied to both BCDI and spBCDI datasets. Note, however, that with speckle illuminations, there are multiple shifted copies of the Bragg peak complex-valued amplitude in the scanned volume. Therefore, we observed that the total number of diffracted photons might be in some cases two times larger than for plane-wave BCDI where there is only one Bragg peak, for the same SNR value. The effect of finite SNR in the diffracted intensity is summarized in Fig. 7. It presents the 3D intensity distribution around the Bragg peak [see Fig. 7(a)], located at $\mathbf{G}_{HKL}$, within an orthogonal reference frame $(\mathbf{Q_x}, \mathbf{Q_y}, \mathbf{Q_z})$, which differs from the tilted detection space $(\tilde{\mathbf{k}}_1, \tilde{\mathbf{k}}_2, \tilde{\mathbf{k}}_3)$ used in Figs. 1–5, because it is the conjugated version of the set of vectors $(\mathbf{x}, \mathbf{y}, \mathbf{z})$ in which the 3D object is represented in Fig. 6. Panels (b), (c), and (d) display the normalized intensity distribution in the three main planes of the reciprocal space, first in the noiseless case infinite (SNR) and then at SNRs of 500 and 200 maximum counts per pixel, respectively.

A performance comparison with the standard BCDI is also included; in this case, the simulations use a plane wave, i.e., a fully homogeneous illumination of the sample. The 3D diffraction pattern is produced for $\sigma_{RC} = 4$, and the binary mask is applied to adjust the (effective) sampling step δ_q along RC. Noise is added to the dataset at a SNR level of 2000 or 1000 expected counts. To quantitatively evaluate the reduction in measurement time produced by speckle BCDI, *a gain factor*

is defined as the ratio between the total intensity (i.e., the total number of photons integrated in the whole volume of the probed reciprocal space) needed to produce a reconstruction from plane-wave BCDI and spBCDI datasets,

$$\text{Gain} \equiv \frac{I_{tot}^{pw}(\sigma = 2, \text{SNR} = 2000)}{I_{tot}^{sp}(\sigma, \text{SNR})} \qquad (7)$$

where $I_{tot}^{pw}(\sigma = 2, \text{SNR} = 2000)$ is the total intensity in a plane-wave BCDI scan for an oversampling ratio along the RC $\sigma = 2$ and for an SNR level of 2000 (this choice as a reference for the standard BCDI is justified by our results of the numerical tests described below). Similarly, $I_{tot}^{sp}(\sigma, \text{SNR})$ is the total intensity in the full speckle BCDI dataset, for any σ and SNR values.

Finally, we also stress that solving the phase retrieval problem in standard BCDI (i.e., with a plane-wave illumination) is much more difficult than solving it for spBCDI. The reconstruction strategy in standard BCDI requires usually that one alternates several times between the error reduction (ER) and the hybrid input-output (HIO) solvers [60,61]. Such an heuristic approach is often tricky to tune. In comparison, spBCDI performs the reconstruction *via* a straightforward adaptation of the ER update (see next section), resulting in a simpler algorithmic strategy.

Table II summarizes the main characteristics of the presented results. It includes the total number of diffraction patterns forming each dataset and the gain in acquisition time, when successful reconstructions are achieved. To evaluate the reliability of the solution obtained by the algorithm, we perform for each condition (i.e., for a given SNR value and σ value) at least 10 reconstructions, starting from an object with random phases. We consider that a reconstruction is reliable when 10 out of 10 reconstructed objects match the original object (here, we decide that a reconstruction matches the original
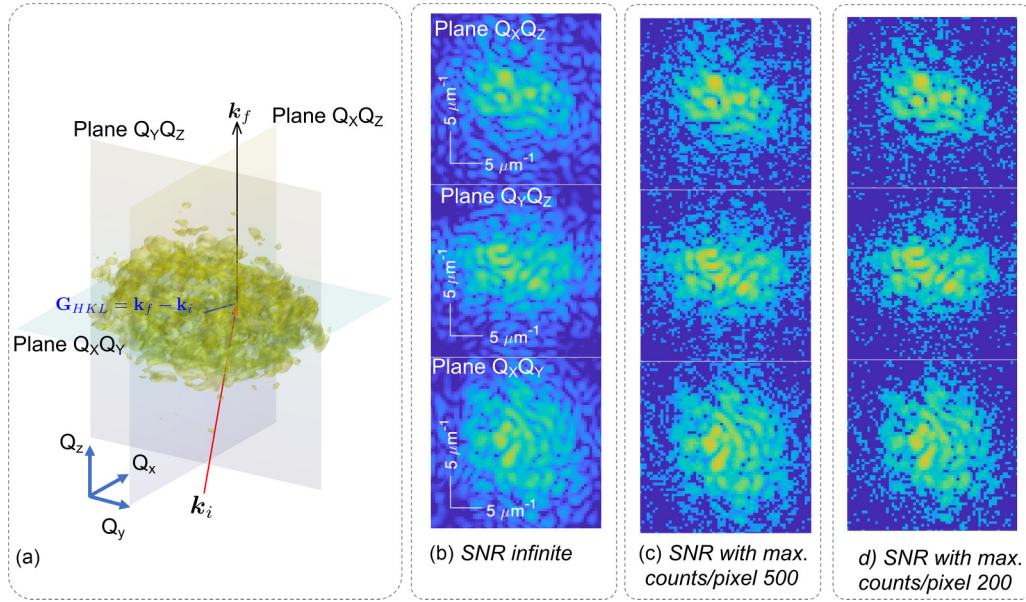
FIG. 7. (a) Normalized 3D diffracted intensity distribution around the *HKL* Bragg peak (located at the head of the Bragg vector $\mathbf{G}_{HKL}$, matching the momentum transfer arising from the vectorial combination of the incoming $\boldsymbol{k}_i$ and outgoing $\boldsymbol{k}_f$ wavevectors) and the three main planes of the reciprocal space. (b)–(d) 2D cuts of the distribution of intensity in the planes highlighted in (a) at infinite SNR first, and then at the two SNRs under study: 500 and 200 maximum counts per pixel respectively. The detector planes corresponds to the (Q_X, Q_Y) plane.

TABLE II. Summary of the performances of spBCDI compared to BCDI for different SNR and σ_{RC} values. Nonreliable (NR) reconstructions are indicated (see main text for definition). They evidence the limit of the method along a given investigated parameter. A gain estimator is introduced in order to quantify the performances when the reconstruction is successful. It corresponds to the ratio between the number of photons in the reference BCDI reconstruction (i.e., SNR = 2000 and $\sigma_{RC} = 2$) and the total number of photons in the spBCDI dataset. Uncolored cells correspond to a gain of 1. Green (resp. orange) cells correspond to a gain larger (resp. smaller) than 1. Gray cells correspond to unsuccessful experimental configurations. The total number of photons in each dataset, Tot. Int., is given; all intensity values are indicated in counts unit. Tests which would not bring any additional information are indicated with "–".

Experiment			σ_{RC}								
	SNR		4	2	1	0.7	0.5	0.4	0.3	0.1	0.06
BCDI $\theta = 9°$ 1 RC	2000	DPs	90	45	23						
		Tot. Int.	$2.2{\times}10^6$	$1.1{\times}10^6$	$5.5{\times}10^5$	–	–	–	–	–	–
		Gain	0.5	1	NR						
	1000	DPs	90	45							
		Tot. Int.	$1.1{\times}10^6$	$5.5{\times}10^5$	–	–	–	–	–	–	–
		Gain	1	NR							
spBCDI $\theta = 9°$ 4 RCs	500	DPs	360	180	92	64	48	36			
		Tot. Int.	$4{\times}10^6$	$2{\times}10^6$	$1{\times}10^6$	$6.8{\times}10^5$	$5.2{\times}10^5$	$3.6{\times}10^5$	–	–	–
		Gain	0.3	0.6	1	1.6	2	NR			
	200	DPs	360	180	92	64	48	36			
		Tot. Int.	$2{\times}10^6$	$1{\times}10^6$	$5.2{\times}10^5$	$3.4{\times}10^5$	$2.6{\times}10^5$	$2{\times}10^5$	–	–	–
		Gain	0.6	1	2	3	4	NR			
spBCDI $\theta = 45°$ 4 RCs	200	DPs	–	–			200		118	40	24
		Tot. Int.	–	–	–	–	$5.2{\times}10^5$	–	$3{\times}10^5$	$1{\times}10^5$	$6{\times}10^4$
		Gain					2		4	11	NR
	100	DPs	–				200			40	24
		Tot. Int.	–	–	–	–	$2.6{\times}10^5$	–	–	$5.2{\times}10^4$	$3{\times}10^4$
		Gain					4			22	NR
	70	DPs					200			40	24
		Tot. Int.	–	–	–	–	$1.3{\times}10^5$	–	–	$2.6{\times}10^4$	$1.5{\times}10^4$
		Gain					9			43	NR
	35	DPs					200		118	40	
		Tot. Int.	–	–	–	–	$6.4{\times}10^4$	–	$3.8{\times}10^4$	$1.3{\times}10^4$	–
		Gain					17		30	NR	

object when the absolute magnitude of the normalized cross correlation is larger that 0.5). See the SM for more details [46]. For very favorable cases (i.e., $\sigma_{RC} > 0.5$ and known support) a reduced number of successful tests (about 3 to 5) is sufficient to evaluate the reliability of the reconstructions. Nonreliable (NR) reconstructions are the ones, which do not fulfill this criterion. Finally, as our aim is to define the limits under which the method yields trustful reconstructions, we estimate there was no need to test either very favorable or more stringent conditions. These cases are indicated with "–".

B. Phase-retrieval strategy in speckle-BCDI

The inversion of the spBCDI simulated measurements was performed with a straightforward adaptation of the traditional *error reduction* (ER) algorithm [60]. More specifically, we define the following criterion to minimize:

$$J(\rho) = \sum_{p=1}^{P} \sum_{n=1}^{N} \Omega(\boldsymbol{q}_n; \sigma_{RC}) \left(\sqrt{\widehat{I_p(\boldsymbol{q}_n)}} - \sqrt{\bar{I}_p(\boldsymbol{q}_n; \rho)} \right)^2. \quad (8)$$

In this relation, $\widehat{I_p(\boldsymbol{q}_n)}$ is the 3D experimental intensity generated from the RC using the pth position of the speckled beam at each pixel $\boldsymbol{q}_n$ of the sampled volume; $\bar{I}_p(\boldsymbol{q}_n; \rho)$ is the noise-free intensity expected for this measurement when the sample ρ is given, see Eq. (2). For a given sampling ratio along the RC, $\Omega(\boldsymbol{q}_n; \sigma_{RC})$ is the 3D binary mask selecting the appropriate set of diffraction patterns within the RC that are considered to run the algorithm. With this error metric, a gradient with respect to ρ is derived and used in an iterative minimization algorithm to estimate the sample [62]. The retrieved object corresponds to a local minimum of the error metric and the algorithm stops when the experimental and calculated diffraction patterns are congruent within the noise level.

We first investigate the reliability of the reconstructions when the object shape is perfectly known; in this case, only ER iterations as described above are sufficient to compute the modulus and phase estimates for each pixel within the known support. When the support is unknown, we need to periodically update the support *via* the shrink-wrap (SW) method [63]; this case will be considered later in this section. In all cases we assume that the speckle illumination (in modulus and phase), and its exact position for each RC scan are perfectly known.

Performances with respect to plane-wave BCDI. To start with, we compare the performances of spBCDI with respect to plane-wave BCDI. The comparison is done at a shallow incidence angle of $9°$, a configuration for which the decrease in σ_{RC}^{min} is expected to be limited [see Eq. (6) and Table I]. Figure 8 summarizes the reconstruction tests performed for a series of datasets consisting in four spBCDI RC scans at shifted beam positions. In these simulations, σ_{RC} varies from the initial value of 4 down to 0.3 and SNR values are set to 500 and 200 counts, respectively. We further assume that the support of the object is exactly known, i.e., the most favorable condition to set a benchmark. To display the results in a single figure, only the reconstructed moduli and phases in the scattering plane (XZ) are presented. Note that for each case, multiple reconstructions were performed to investigate

the robustness of the inversion and the reliability of the obtained results. While BCDI starts failing for $\sigma_{RC} \leqslant 2$ at a SNR of 2000 counts and even for $\sigma_{RC} \leqslant 4$ for an SNR of 1000 counts (see Table II), the spBCDI approach still provides reliable reconstructions for a σ_{RC} value down to 0.5, for the two investigated SNRs. A more detailed description regarding the reconstruction quality, is shown in Fig. 9, which presents the retrieved moduli and phases for three different planes, in four selected cases: standard BCDI at $\sigma_{RC} = 2$ and SNR of 2000, and three spBCDI reconstructions at SNR of 200 for σ_{RC} values of 2, 0.5, and 0.3. It demonstrates the great fidelity achieved in spBCDI reconstructions, specially regarding the retrieved phase, at a very low σ_{RC} of 0.5, which is well below the usual value established by the Shannon-Nyquist theorem, and slightly below the expected minimal value of 0.64 given in Table I. As often observed in presence of noise in the intensity patterns, the reconstruction of the modulus is more challenging at finite SNR [41]. However, despite of a degraded modulus reconstruction, inversion of spBCDI datasets successfully retrieves the phase in this heavily distorted crystal and even with a reduced number of diffraction patterns (Table II). An empirical limiting value of $\sigma_{RC} = 0.4$ is found, which corresponds to the limit from which the algorithm fails systematically to reconstruct neither the modulus nor the phase [see Fig. 9(d) where the reconstruction at $\sigma_{RC} = 0.3$ is presented]. In this specific case, accounting for the four RC scans per dataset in spBCDI, a σ_{RC} of 0.4 and a SNR of 200 yields a measurement time of a factor 4 shorter than for the standard plane-wave BCDI dataset simulated at $\sigma_{RC} = 2$, i.e., the minimum σ_{RC} value needed to provide a reasonable estimate of the distorted phase field for an SNR of 2000. This gain represents already a significant reduction of the acquisition time.

Impact of a partially known support. The performance of the spBCDI approach when the support is unknown is also analyzed. Figure 10 shows a series of 3D reconstructions obtained when the initial support is not perfectly known. By incorporating the SW routine [63], the capability of the reconstruction algorithm to retrieve the phase and the shape of the cubic crystal from a spBCDI dataset is further examined. The initial support size is set to 1.5 times the object size, and its contour is shown in white in the phase cuts. Successful reconstructions are obtained for spBCDI datasets of $\sigma_{RC} \geqslant 0.5$, as in the previous known support case. Note that, for $\sigma_{RC} = 0.5$, we need to slightly reduce the initial support size to 1.3 times the object size. Thus, provided that we have a partial knowledge of the support, gathered from previous measurements at higher σ_{RC} or other images from electronic microscopy or AFM, the ER/SW algorithms can be used successfully with strongly undersampled spBCDI datasets, with similar performances as the ones discussed in the previous paragraph.

Impact of the incidence angle. The other extreme case, i.e., the large incident angle configuration, is herein investigated. In this new series of tests (summarized in Fig. 11), an incident angle of $45°$ is chosen. As explained in Sec. III A, to enable the exploration of drastically reduced σ_{RC}, the direct-space pixel size along the RC direction is decreased by a factor of 3 (yielding a pixel size of $\sim$10 nm in the RC direction). Thereby, even with small σ_{RC} values, the
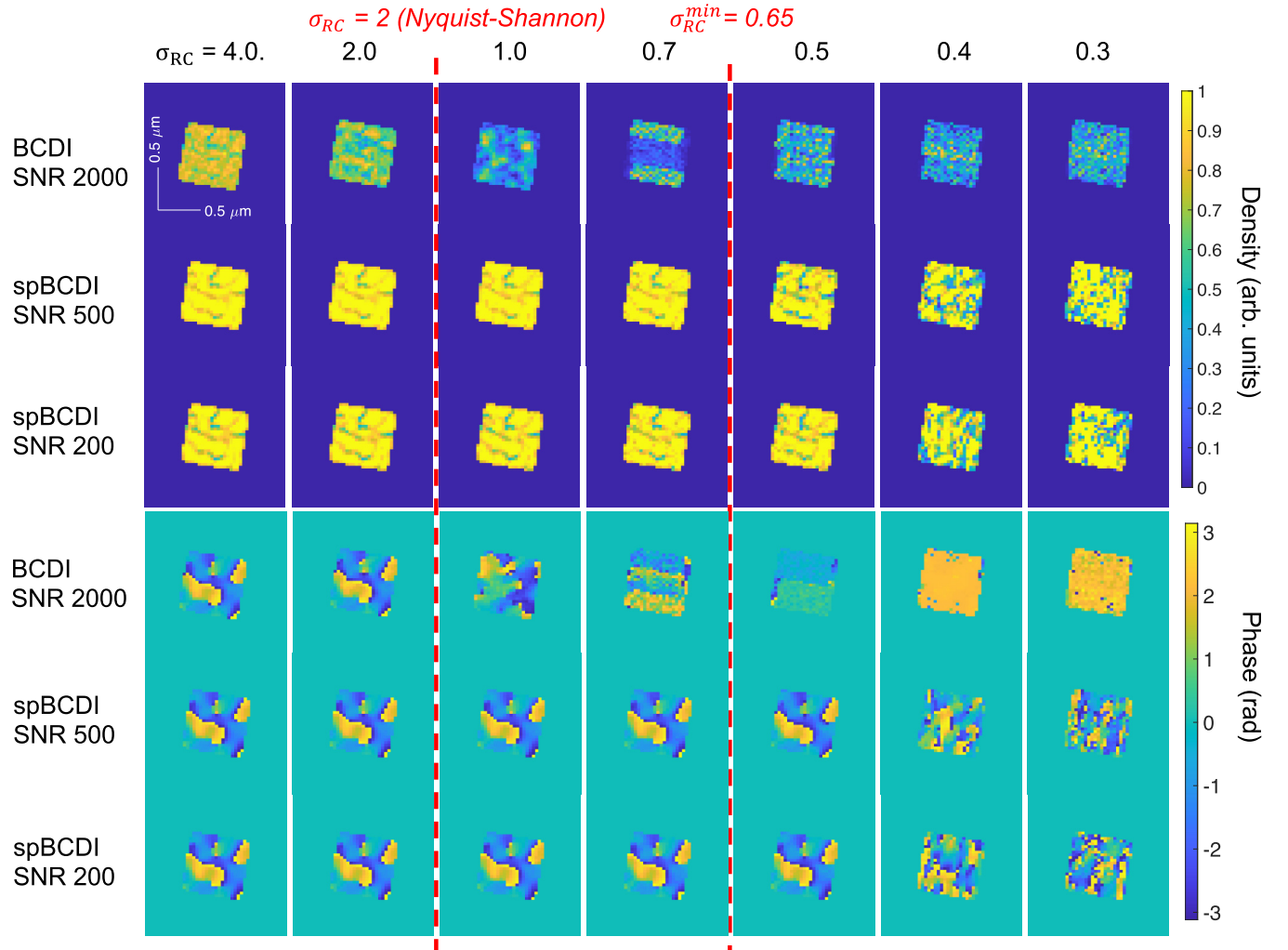
FIG. 8. Speckle BCDI (spBCDI) vs standard plane-wave BCDI. A comparison study for $\theta_B = 9°$. Reconstruction results are shown for different sampling ratio σ_{RC} and different SNR levels. To avoid regions of zero photon deposit for speckle illumination, each spBCDI dataset consists of a series of four RC scans taken at shifted positions of the beam. These tests assume a known support for the sample.

downsampled dataset still contains DPs to properly guide the algorithm. Roughly, for $\sigma_{RC} = 2$, the total number of diffraction patterns for one full spBCDI dataset is about 800. Results presented in Fig. 11 show that spBCDI still succeeds to provide reliable reconstructions for σ_{RC} down to 0.1, corresponding to the theoretical limit given by Eq. (6) and reported in Table I. For an SNR value of 200, it corresponds to a gain of about 11, which corresponds to a three times shorter acquisition time than achieved for spBCDI at 9° (Table II).

Impact of SNR. The wide angle configuration (i.e., the 45° incident angle geometry) is further used to provide an interesting exploration of the limits of the method with respect to very low SNR and σ_{RC} levels. In this last series of tests, SNRs ranging from 100 down to 35 counts are introduced. As observed from the main results presented in Fig. 11, spBCDI still performs successfully down to the theoretical limit of $\sigma_{RC} = 0.1$ for SNRs as low as 70 counts. It starts degrading at lower SNRs ($\leqslant 35$ counts), which requires an increase of the σ_{RC} value (up to 0.3) to achieve a reasonable reconstruction of the phase. In these last tests, the best achievable gain, with respect to BCDI, is of the order of 43 (Table II). This means

that the acquisition time can be drastically reduced, opening significant opportunities for experimental applications.

IV. DISCUSSION

This paper presents an approach for performing BCDI microscopy with a speckle illumination. The structured beam, which, in the reciprocal space, produces a mix of information along the RC direction allows to overcome two important limits of traditional BCDI: (i) the need for high sampling frequencies along the RC scanning direction to ensure the robustness of the phase reconstruction for highly nonhomogeneously strained crystal; (ii) the long acquisition times, which precludes the imaging of time evolving crystals. To show the performance of the method, we have focused on a symmetric Bragg reflection, ensuring the simplicity of the simulations. But the same results are expected for a nonsymmetric reflection, as long as the detector plane is significantly nonperpendicular to the beam direction (i.e., for incident angles $\geqslant 10°$). Our results confirm that the minimum sampling ratio is decreasing for larger incident angles and smaller
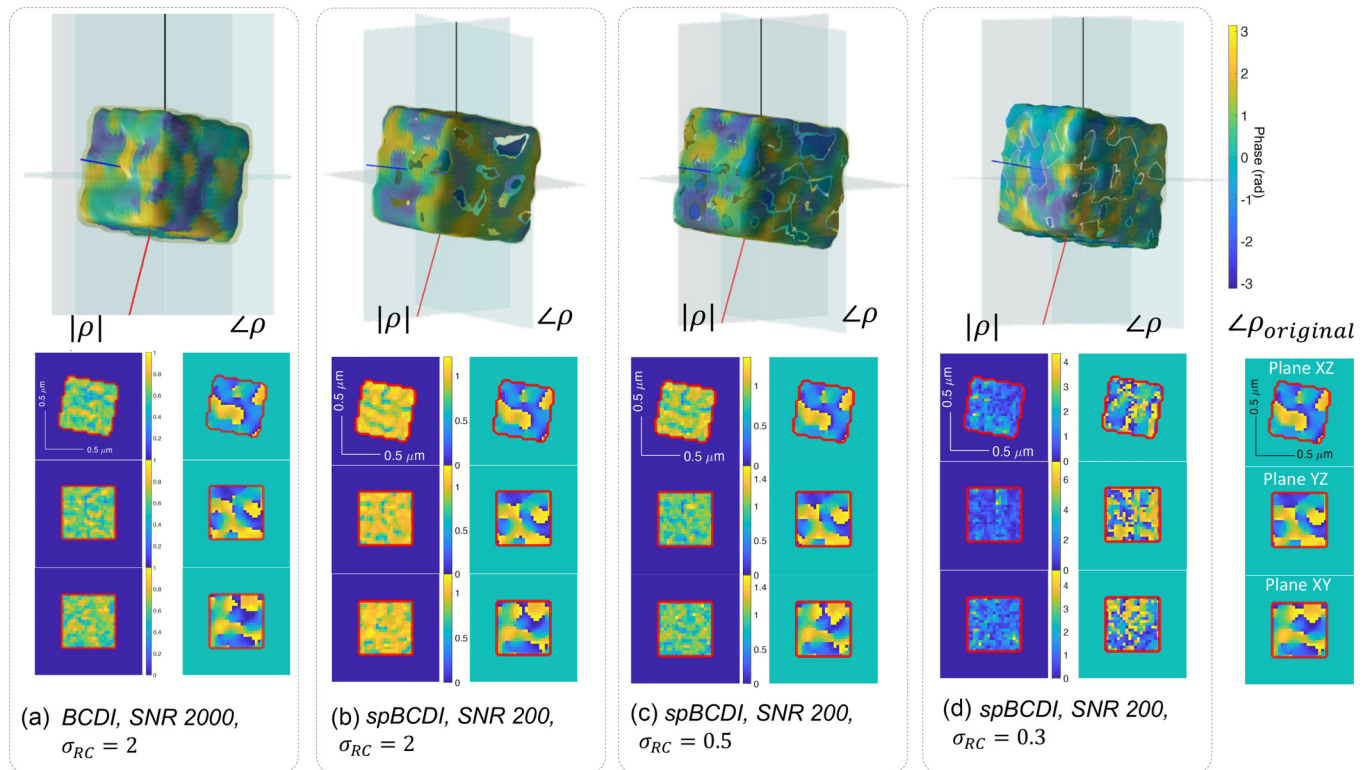
FIG. 9. 3D reconstructions of BCDI (a) and spBCDI (b)–(d) datasets when the support is exactly known, for $\theta_B = 9°$. The modulus $|\rho|$, and the phase $\angle\rho$, of the object are shown while the contour of the support is indicated in red. This latter is also shown in the 3D pictures with a semitransparent yellow surface. Each column from (a) to (d) contains a label, which specifies the RC sampling frequency σ_{RC}, and the SNR values.

speckle sizes, as established in Eq. (6). Furthermore, the use of spBCDI allows working at extremely small SNR, showing that an efficient use of the diffracted photons is obtained with speckle illumination. Typically, a reduction of a factor of about 50 in SNR is observed between BCDI and spBCDI. Therefore, although spBCDI requires the acquisition of multiple RC scans performed at slightly shifted positions to avoid zero photon deposit regions, the gain with respect to acquisition time and the performances of spBCDI with respect to distorted crystals are large enough to justify its experimental implementation.

Regarding the gain with respect to the sampling direction, which is directly related to the total acquisition time, we observe that for individual speckle sizes of ~50 nm, σ_{RC} can be reduced down to 0.1 (resp. 0.5) for an incident angle of 45° (resp. 9°), while BCDI requires a σ_{RC} value of at least 2. This corresponds to a gain in sampling frequency of 20 (resp. 4) along the rocking curve. However, this first estimate does not account for the possibility to drastically reduce the SNR level, as observed in Fig. 11 and Table II. Indeed, a gain in acquisition time of about 43 is reached for an SNR as small as 70 counts, to be compared to the needed SNR of 2000 counts for BCDI, in the case of highly distorted crystal. Transposing these numbers to experimental parameters provides an estimate of the typical accessible time scales at fourth-generation synchrotrons. In a previous paper [30], a typical acquisition time of about 33 ms for an SNR of 280 counts was reported. It would correspond to a total acquisition time of 11 s for a BCDI dataset of 45 diffraction patterns and an SNR of 2000

counts, as introduced in the present paper. For the low SNR regime, this acquisition time may decrease down to about 0.2 s for spBCDI. Thus, spBCDI will highly benefit from the very small (e.g., ~30–50 nm) and brilliant beams generated at new fourth-generation light sources [64,65]. Note that this preliminary estimation does not account for the time needed to move the different scanning motors (specially the rocking motors), which will become limiting factors for temporal resolution. However, we anticipate that additional gains could be obtained by shifting the angular positions by less than one angular step or to use continuous rotation schemes based on flyscans [66], for each of the four RC. This partial overlapping in reciprocal space should still contain enough information to allow for additional reduction of the sampling conditions with speckle beams.

Regarding the gain for imaging complex crystalline samples, the present test would correspond to a strain distribution with a total extent of almost 10^{-2}, with most of the nonhomogeneous strain distribution included in a range of about 10^{-3} and a small portion of the distribution reaching an amplitude of $\sim \pm 4 \times 10^{-3}$ (see the SM [46]). Such a strain distribution compares well to experimental strain fields in experimental works by Ulvestad *et al.* [6] in the study of topological defects in battery grains or by Sun *et al.* [67] within single grains in solid-state electrolytes. These studies reported strain amplitudes of 4×10^{-3} and even larger (7×10^{-3}). Remarkably, spBCDI keeps on performing well even at low SNR, which is not the case for BCDI, as observed when reducing the SNR by a factor of 2, from 2000 counts to 1000 counts (Table II).
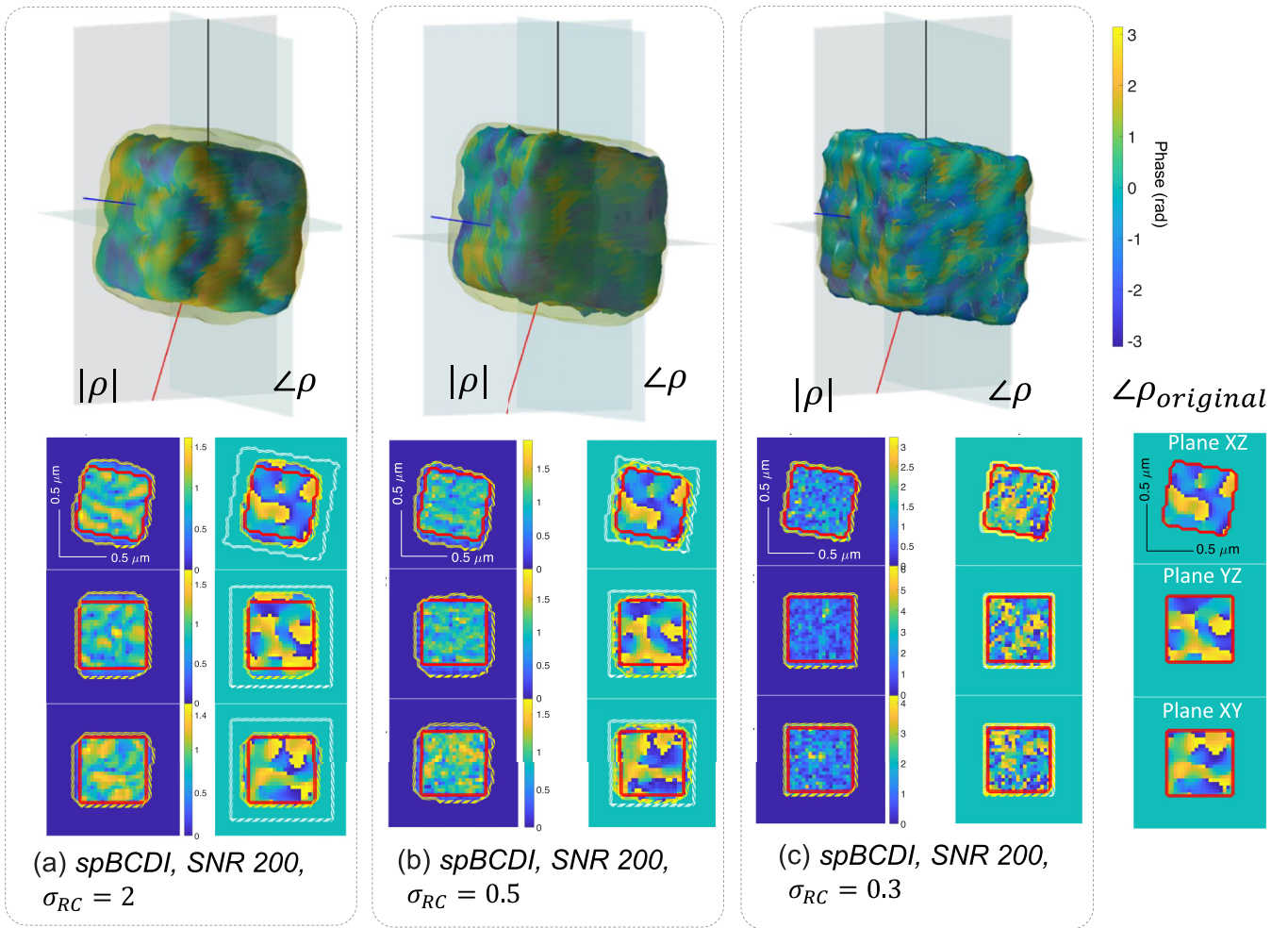
FIG. 10. 3D reconstructions for spBCDI datasets when SW is used (i.e., the exact support is unknown), for $\theta_B = 9°$. For each reconstruction, the modulus $|\rho|$ and the phase $\angle\rho$, of the object are shown. The initial support contour is indicated by a white-dotted line, while the yellow line delineates the finally obtained support. It is also displayed in the 3D pictures with a semitransparent yellow isosurface. Finally, the exact support contour is marked in red. Each column contains a label, which specifies the RC sampling frequency σ_{RC}, and the SNR value.

While the scope of this paper is to numerically establish the relevance of spBCDI, the experimental demonstration is desirable. Practically, the implementation of the proposed approach requires to discuss the needs for the modulator phase plate (MPP) production, the coupling of the phase plate with the focusing optics, the scanning stage and the diffractometer. The MPP can be produced by two-photon lithography [68,69] of an x-ray phase shifting polymer. The typical size of domains, which present rather homogeneous phase directly drives the beam envelope size. Our estimation, presented in Fig. 3, shows that these domains, in the 1–10 micrometer range, are compatible with present printing technologies. When needed, the domain size can be easily adapted to the crystal size, ensuring that most of the photons at the focal plane illuminate the sample. This strategy is in contrast to standard BCDI, based on plane-wave illumination and where only the central part of the beam is used.

The MPP, which shapes the illumination, should be installed close to the focusing optics. Thereby, it benefits from the stable environment surrounding the optics. As a result, the beam produced by the combination of the phase plate and the focusing optics is weakly sensitive to their relative vibration, as the wave-field close to the focusing element is only weakly structured. The phase plate positioning, alignment and characterization can be performed on the forward geometry, without the need for the crystalline sample.

Besides the specificity regarding the illumination, the spBCDI set-up is rather similar to the Bragg ptychography set-up, which is available at several synchrotrons worldwide [27,30,47,54,70]. This includes a scanning translation stage and a diffractometer for crystalline alignment without further modification. In addition, it has been recently proven that illumination description (i.e., amplitude and phase) and position along the rocking curve can be retrieved in a Bragg ptychography experiment [27,30], which should ease the implementation of this method.

Finally, we note that Zhao *et al.* [22] have recently proposed to perform BCDI with a modulator, presenting some similarities with our spBCDI method. Their approach, which
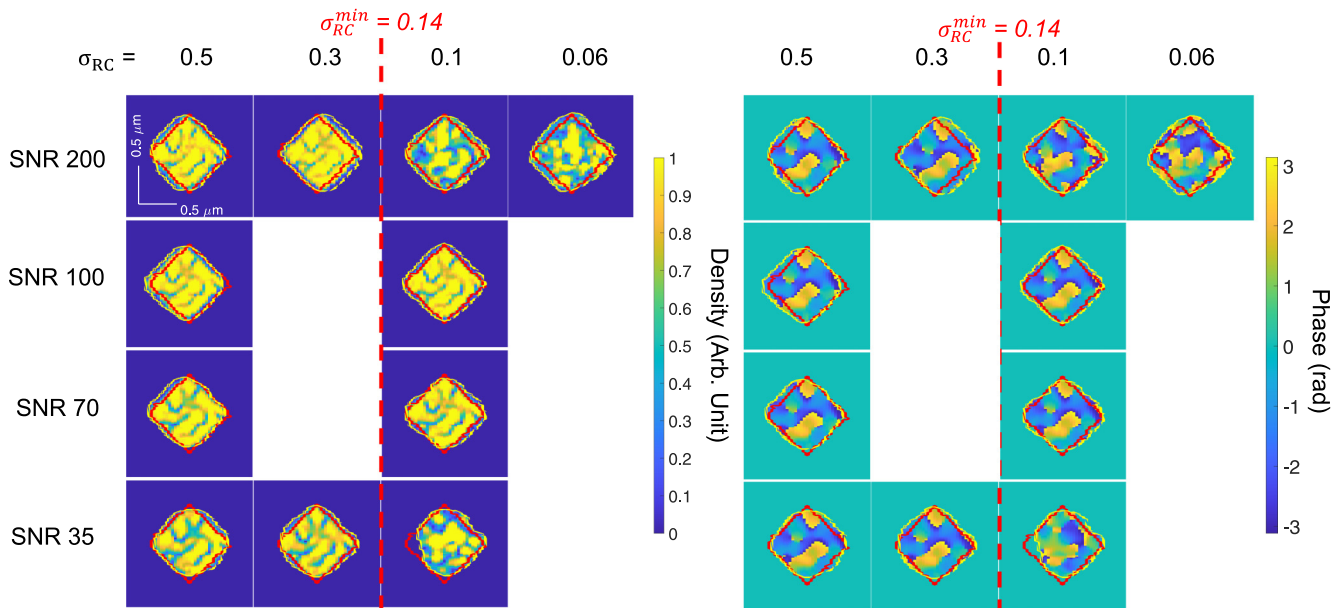
FIG. 11. Cut across the scattering plane of the 3D reconstructions for spBCDI datasets when SW is used (i.e., the exact support is unknown), for $\theta_B = 45°$. For each reconstruction, the modulus $|\rho|$ (left) and the phase $\angle\rho$ (right) of the object are shown. The yellow line delineates the contour of the finally obtained support to be compared to the exact support contour, marked in red. The used σ_{RC} (columns) and the SNR levels (lines) are specified in the figure.

aims at pushing further the capabilities of BCDI for highly distorted crystalline samples, consists in placing the modulator after the sample and parallel to the detector plane. Thereby, they increase substantially the spatial resolution achieved in each slice of the RC scan, yielding datasets with sufficient constraints to produce a robust and unique image of the crystal phase domains. However, because the modulation of the exit-field does not mix the information along the RC scan, the ability to relax the sampling conditions is not expected. This is a key difference with our proposed spBCDI. The practical implementation is also rather different as the phase plate should be placed close to the sample, involving additional constraints with respect to spBCDI.

V. SUMMARY AND CONCLUSIONS

This paper proposes a methodology in the framework of coherent x-ray microscopy, spBCDI, based on a strongly nonuniform illumination or *speckle illumination*. Thereby, we increase the efficiency with which the reciprocal space is sampled and drastically diminish the measurement times. We describe the theoretical foundations of the new method, predicated on the definition of the diffracted wave field as a convolution between the object and the illumination FT. By altering the illumination, we produce shifted copies of the physically observable region (i.e., the Bragg peak) and enable the sampling of extra information, which would be inaccessible with plane-wave illumination. Thus, speckle illumination produces a multiplexing of the Bragg peak, and hence, a noticeable reduction in the oversampling ratio along the RC scan σ_{RC}. Besides, we provide a qualitative rule, which connects the experimental parameters (i.e., incident angle and speckle size) to the minimum σ_{RC} above which the dataset

can be inverted, yielding a robust and unique reconstruction of the object's phase. Numerical investigations show that values of σ_{RC} as small as 0.1 could be reached, to be compared to the Nyquist-Shannon requirement of $\sigma_{RC} = 2$ for standard (plane-wave) BCDI. The observed reduction in SNR leads to a decrease of total acquisition time by a factor of 40. Finally, some details regarding the practical implementation of the method at synchrotron sources are discussed, including the experimental methodology to design a speckle illumination, fully characterized by a specific speckle size and an envelop determining the field of view. The unprecedented performances at fourth-generation synchrotron sources, coupled to the enhanced efficiency of spBCDI measurements, open exciting experimental avenues, to access the wide range of time and length scales associated to different structural drivers for, e.g., crystal dissolution or growth in liquid medium [71–73], crystal damages under x-ray illumination [74], nanoparticles annealing [75], morphological and internal structure changes upon catalysis [76].

We conclude that spBCDI offers an attractive alternative approach to traditional plane-wave BCDI, which combines faster measurement with the ability of imaging strongly distorted crystals, even at low SNR levels. Typically at fourth-generation synchrotron sources, total acquisition times in the order of 0.2 s could be reached. Our next step is to apply spBCDI to dynamic crystalline systems. We believe that the possibility of imaging dynamic crystals will appeal a wide variety of scientific communities, including physicists, chemists, geologists, biologists, or materials scientists. Finally, the new capabilities of fourth-generation light sources will promote these techniques to observe the evolution of crystalline matter *in situ* and under realistic conditions. Therefore, we expect that spBCDI will be readily adopted in these new radiation

sources, which are becoming more and more available all over the world.

[1] I. Robinson and R. Harder, Coherent x-ray diffraction imaging of strain at the nanoscale, Nat. Mater. **8**, 291 (2009).

[2] M. A. Pfeifer, G. J. Williams, I. A. Vartanyants, R. Harder, and I. K. Robinson, Three-dimensional mapping of a deformation field inside a nanocrystal, Nature (London) **442**, 63 (2006).

[3] W. Cha, A. Ulvestad, M. Allain, V. Chamard, R. Harder, S. J. Leake, J. Maser, P. H. Fuoss, and S. O. Hruszkewycz, Three dimensional variable-wavelength x-ray Bragg coherent diffraction imaging, Phys. Rev. Lett. **117**, 225501 (2016).

[4] J. Miao and D. Sayre, On possible extensions of x-ray crystallography through diffraction-pattern oversampling, Acta Cryst. A **56**, 596 (2000).

[5] C. Atlan, C. Chatelier, I. Martens, M. Dupraz, A. Viola, N. Li, L. Gao, S. J. Leake, T. U. Schülli, J. Eymery *et al.*, Imaging the strain evolution of a platinum nanoparticle under electrochemical control, Nat. Mater. **22**, 754 (2023).

[6] A. Ulvestad, A. Singer, J. N. Clark, H. M. Cho, J. W. Kim, R. Harder, J. Maser, Y. S. Meng, and O. G. Shpyrko, Topological defect dynamics in operando battery nanoparticles, Science **348**, 1344 (2015).

[7] S. Choi, M. Chung, D. Kim, S. Kim, K. Yun, W. Cha, R. Harder, T. Kawaguchi, Y. Liu, A. Ulvestad *et al.*, In situ strain evolution on pt nanoparticles during hydrogen peroxide decomposition, Nano Lett. **20**, 8541 (2020).

[8] K. Yuan, S. S. Lee, W. Cha, A. Ulvestad, H. Kim, B. Abdilla, N. C. Sturchio, and P. Fenter, Oxidation induced strain and defects in magnetite crystals, Nat. Commun. **10**, 703 (2019).

[9] J. N. Clark, J. Ihli, A. S. Schenk, Y.-Y. Kim, A. N. Kulak, J. M. Campbell, G. Nisbet, F. C. Meldrum, and I. K. Robinson, Three-dimensional imaging of dislocation propagation during crystal growth and dissolution, Nat. Mater. **14**, 780 (2015).

[10] J. Ihli, J. N. Clark, N. Kanwal, Y.-Y. Kim, M. A. Holden, R. J. Harder, C. C. Tang, S. E. Ashbrook, I. K. Robinson, and F. C. Meldrum, Visualization of the effect of additives on the nanostructures of individual bio-inspired calcite crystals, Chem. Sci. **10**, 1176 (2019).

[11] I. Robinson, T. A. Assefa, Y. Cao, G. Gu, R. Harder, E. Maxey, and M. P. M. Dean, Domain texture of the orthorhombic phase of $La_{2−x}Ba_xCuO_4$, J. Supercond. Nov. Magn. **33**, 99 (2020).

[12] X. Huang, R. Harder, G. Xiong, X. Shi, and I. Robinson, Propagation uniqueness in three-dimensional coherent diffractive imaging, Phys. Rev. B **83**, 224109 (2011).

[13] S. Maddali, P. Li, A. Pateras, D. Timbie, N. Delegan, A. L. Crook, H. Lee, I. Calvo-Almazan, D. Sheyfer, W. Cha *et al.*, General approaches for shear-correcting coordinate transformations in Bragg coherent diffraction imaging. Part I, J. Appl. Cryst. **53**, 393 (2020).

[14] G. Xiong, O. Moutanabbir, M. Reiche, R. Harder, and I. Robinson, Coherent x-ray diffraction imaging and characterization of strain in silicon-on-insulator nanostructures, Adv. Mater. **26**, 7747 (2014).

[15] H. Öztürk, X. Huang, H. Yan, I. K. Robinson, I. C. Noyan, and Y. S. Chu, Performance evaluation of Bragg coherent diffraction imaging, New J. Phys. **19**, 103001 (2017).

[16] A. Ulvestad, A. Tripathi, S. O. Hruszkewycz, W. Cha, S. M. Wild, G. B. Stephenson, and P. H. Fuoss, Coherent diffractive imaging of time-evolving samples with improved temporal resolution, Phys. Rev. B **93**, 184105 (2016).

[17] L. Wu, P. Juhas, S. Yoo, and I. Robinson, Complex imaging of phase domains by deep neural networks, IUCrJ **8**, 12 (2021).

[18] X. Chen, S. Zhong, Y. Hou, R. Cao, W. Wang, D. Li, Q. Dai, D. Kim, and P. Xi, Superresolution structured illumination microscopy reconstruction algorithms: A review, Light Sci. Appl. **12**, 172 (2023).

[19] E. Mudry, K. Belkebir, J. Girard, J. Savatier, E. Le Moal, C. Nicoletti, M. Allain, and A. Sentenac, Structured illumination microscopy using unknown speckle patterns, Nat. Photon. **6**, 312 (2012).

[20] M. G. L. Gustafsson, Surpassing the lateral resolution limit by a factor of two using structured illumination microscopy, J. Microsc. **198**, 82 (2000).

[21] R. Fiolka, L. Shao, E. H. Rego, M. W. Davidson, and M. G. L. Gustafsson, Time-lapse two-color 3D imaging of live cells with doubled resolution using structured illumination, Proc. Natl. Acad. Sci. USA **109**, 5311 (2012).

[22] J. Zhao, I. A. Vartanyants, and F. Zhang, Bragg coherent modulation imaging for highly strained nanocrystals: A numerical study, J. Appl. Cryst. **56**, 1528 (2023).

[23] F. Zhang, B. Chen, G. R. Morrison, J. Vila-Comamala, M. Guizar-Sicairos, and I. K. Robinson, Phase retrieval by coherent modulation imaging, Nat. Commun. **7**, 13367 (2016).

[24] A. M. Maiden, G. R. Morrison, B. Kaulich, A. Gianoncelli, and J. M. Rodenburg, Soft x-ray spectromicroscopy using ptychography with randomly phased illumination, Nat. Commun. **4**, 1669 (2013).

[25] G. R. Morrison, F. Zhang, A. Gianoncelli, and I. K. Robinson, X-ray ptychography using randomized zone plates, Opt. Express **26**, 14915 (2018).

[26] M. Guizar-Sicairos, M. Holler, A. Diaz, J. Vila-Comamala, O. Bunk, and A. Menzel, Role of the illumination spatial-frequency spectrum for ptychography, Phys. Rev. B **86**, 100103(R) (2012).

[27] P. Li, N. W. Phillips, S. Leake, M. Allain, F. Hofmann, and V. Chamard, Revealing nano-scale lattice distortions in implanted material with 3D Bragg ptychography, Nat. Commun. **12**, 7059 (2021).

[28] M. Borland, G. Decker, L. Emery, V. Sajaev, Y. Sun, and A. Xiao, Lattice design challenges for fourth-generation storage-ring light sources, J. Synchrotron Rad. **21**, 912 (2014).

[29] R. Hettel, DLSR design and plans: An international overview, J. Synchrotron Rad. **21**, 843 (2014).

[30] P. Li, M. Allain, T. A. Grünewald, M. Rommel, A. Campos, D. Carbone, and V. Chamard, 4th generation synchrotron source boosts crystalline imaging at the nanoscale, Light Sci. Appl. **11**, 73 (2022).

[31] M. Stockmar, P. Cloetens, I. Zanette, B. Enders, M. Dierolf, F. Pfeiffer, and P. Thibault, Near-field ptychography: phase retrieval for inline holography using a structured illumination, Sci. Rep. **3**, 1927 (2013).

[32] P. Li, D. J. Batey, T. B. Edo, A. D. Parsons, C. Rau, and J. M. Rodenburg, Multiple mode x-ray ptychography using a lens and a fixed diffuser optic, J. Opt. **18**, 054008 (2016).

[33] M. Odstrčil, M. Lebugle, M. Guizar-Sicairos, C. David, and M. Holler, Towards optimized illumination for high-resolution ptychography, Opt. Express **27**, 14981 (2019).

[34] J. Miao, D. Sayre, and H. N. Chapman, Phase retrieval from the magnitude of the Fourier transforms of nonperiodic objects, J. Opt. Soc. Am. A **15**, 1662 (1998).

[35] D. Sayre, Some implications of a theorem due to Shannon, Acta Cryst. **5**, 843 (1952).

[36] P. Li, S. Maddali, A. Pateras, I. Calvo-Almazan, S. Hruszkewycz, W. Cha, V. Chamard, and M. Allain, General approaches for shear-correcting coordinate transformations in Bragg coherent diffraction imaging. Part II, J. Appl. Cryst. **53**, 404 (2020).

[37] The OSR bound Eq. (1) is a sufficient condition ensuring that an essentially unique solution exist for 2D phase retrieval problems; in 3D, this bound can even be slightly relaxed, see [77]. Solving numerically the phase retrieval problem (with a dedicated algorithm) is, however, more difficult and OSR $\sigma > 2$ are typically at use, see [[15], Sec. 3.1] as well as our own simulations in Sec. II.B.a.

[38] M. H. Hayes, *The Unique Reconstruction of Multidimensional Sequences from Fourier Transform Magnitude or Phase" in Image Recovery: Theory and Application*, edited by Henry Stark (Academic Press, New York, 1987).

[39] J. Mertz, *Introduction to Optical Microscopy* (Cambridge University Press, Cambridge, 2019).

[40] J. M. Rodenburg, A. C. Hurst, A. G. Cullis, B. R. Dobson, F. Pfeiffer, O. Bunk, C. David, K. Jefimovs, and I. Johnson, Hard-x-ray lensless imaging of extended objects, Phys. Rev. Lett. **98**, 034801 (2007).

[41] P. Godard, M. Allain, V. Chamard, and J. Rodenburg, Noise models for low counting rate coherent diffraction imaging, Opt. Express **20**, 25914 (2012).

[42] I. A. Vartanyants and I. K. Robinson, Partial coherence effects on the imaging of small crystals using coherent x-ray diffraction, J. Phys.: Condens. Matter **13**, 10593 (2001).

[43] A. Kubec, M.-C. Zdora, U. T. Sanli, A. Diaz, J. Vila-Comamala, and C. David, An achromatic x-ray lens, Nat. Commun. **13**, 1305 (2022).

[44] S. Bajt, M. Prasciolu, H. Fleckenstein, M. Domaracký, H. N. Chapman, A. J. Morgan, O. Yefanov, M. Messerschmidt, Y. Du, K. T. Murray *et al.*, X-ray focusing with efficient high-na multilayer Laue lenses, Light Sci. Appl. **7**, 17162 (2018).

[45] P. Thibault, M. Dierolf, A. Menzel, O. Bunk, C. David, and F. Pfeiffer, High-resolution scanning x-ray diffraction microscopy, Science **321**, 379 (2008).

[46] See Supplemental Material at http://link.aps.org/supplemental/10.1103/PhysRevB.110.134117 for a description of the Bragg geometry, and also, for more details about the simulation of *speckle illumination*, and the calculation of strain tensor components from the complex phase of the object. It also contains the Refs. [1,56–58].

[47] S. O. Hruszkewycz, M. Allain, M. V. Holt, C. E. Murray, J. R. Holt, P. H. Fuoss, and V. Chamard, High-resolution three-dimensional structural microscopy by single-angle Bragg ptychography, Nat. Mater. **16**, 244 (2017).

[48] V. Chamard, M. Allain, P. Godard, A. Talneau, G. Patriarche, and M. Burghammer, Strain in a silicon-on-insulator nanostructure revealed by 3D x-ray bragg ptychography, Sci. Rep. **5**, 9827 (2015).

[49] J. Idier, S. Labouesse, M. Allain, P. Liu, S. Bourguignon, and A. Sentenac, On the superresolution capacity of imagers using unknown speckle illuminations, IEEE Trans. Comput. Imag. **4**, 87 (2018).

[50] K. Jefimovs, O. Bunk, F. Pfeiffer, D. Grolimund, J. van der Veen, and C. David, Fabrication of fresnel zone plates for hard x-rays, Microelectron. Eng. **84**, 1467 (2007).

[51] H. C. Kang, J. Maser, G. B. Stephenson, C. Liu, R. Conley, A. T. Macrander, and S. Vogt, Nanometer linear focusing of hard x rays by a multilayer Laue lens, Phys. Rev. Lett. **96**, 127401 (2006).

[52] A. Snigirev, V. Kohn, I. Snigireva, and B. Lengeler, A compound refractive lens for focusing high-energy x-rays, Nature (London) **384**, 49 (1996).

[53] P. Kirkpatrick and A. V. Baez, Formation of optical images by x-rays, J. Opt. Soc. Am. **38**, 766 (1948).

[54] F. Mastropietro, P. Godard, M. Burghammer, C. Chevallard, J. Daillant, J. Duboisset, M. Allain, P. Guenoun, J. Nouet, and V. Chamard, Revealing crystalline domains in a mollusc shell single-crystalline prism, Nat. Mater. **16**, 946 (2017).

[55] M. C. Newton, Concurrent phase retrieval for imaging strain in nanocrystals, Phys. Rev. B **102**, 014104 (2020).

[56] M. C. Newton, S. J. Leake, R. Harder, and I. K. Robinson, Three-dimensional imaging of strain in a single ZnO nanorod, Nat. Mater. **9**, 120 (2010).

[57] J. Carnis, L. Gao, S. Labat, Y. Y. Kim, J. P. Hofmann, S. J. Leake, T. U. Schülli, E. J. M. Hensen, O. Thomas, and M.-I. Richard, Towards a quantitative determination of strain in Bragg coherent x-ray diffraction imaging: artefacts and sign convention in reconstructions, Sci. Rep. **9**, 17357 (2019).

[58] A. I. Pateras, M. Allain, P. Godard, L. Largeau, G. Patriarche, A. Talneau, K. Pantzas, M. Burghammer, A. A. Minkevich, and V. Chamard, Nondestructive three-dimensional imaging of crystal strain and rotations in an extended bonded semiconductor heterostructure, Phys. Rev. B **92**, 205305 (2015).

[59] P. Geissbühler, P. Fenter, E. DiMasi, G. Srajer, L. Sorensen, and N. Sturchio, Three-dimensional structure of the calcite–water interface by surface x-ray scattering, Surf. Sci. **573**, 191 (2004).

[60] J. R. Fienup, Phase retrieval algorithms: A comparison, Appl. Opt. **21**, 2758 (1982).

[61] S. Marchesini, Invited article: A unified evaluation of iterative projection algorithms for phase retrieval, Rev. Sci. Instrum. **78**, 011301 (2007).

[62] J. Nocedal and S. J. Wright, *Numerical Optimization*, 2nd ed. (Springer, New York, 2006).

[63] S. Marchesini, H. He, H. N. Chapman, S. P. Hau-Riege, A. Noy, M. R. Howells, U. Weierstall, and J. C. H. Spence, X-ray image reconstruction from a diffraction pattern alone, Phys. Rev. B **68**, 140101(R) (2003).

[64] P. Raimondi, C. Benabderrahmane, P. Berkvens, J. C. Biasci, P. Borowiec, J.-F. Bouteille, T. Brochard, N. B. Brookes, N. Carmignani, L. R. Carver *et al.*, The extremely brilliant source storage ring of the european synchrotron radiation facility, Commun. Phys. **6**, 82 (2023).

[65] P. F. Tavares, E. Al-Dmour, Å. Andersson, F. Cullinan, B. N. Jensen, D. Olsson, D. K. Olsson, M. Sjöström, H. Tarawneh, S. Thorin, and A. Vorozhtsov, Commissioning and first-year operational results of the MAXIV 3GeV ring, J. Synchrotron Rad. **25**, 1291 (2018).

[66] P. M. Pelz, M. Guizar-Sicairos, P. Thibault, I. Johnson, M. Holler, and A. Menzel, On-the-fly scans for x-ray ptychography, Appl. Phys. Lett. **105**, 251101 (2014).

[67] Y. Sun, O. Gorobstov, L. Mu, D. Weinstock, R. Bouck, W. Cha, N. Bouklas, F. Lin, and A. Singer, X-ray nanoimaging of crystal defects in single grains of solid-state electrolyte $Li_{7-3x}Al_xLa_3Zr_2O_{12}$, Nano Lett. **21**, 4570 (2021).

[68] F. Seiboth, D. Brückner, M. Kahnt, M. Lyubomirskiy, F. Wittwer, D. Dzhigaev, T. Ullsperger, S. Nolte, F. Koch, C. David *et al.*, Hard x-ray wavefront correction via refractive phase plates made by additive and subtractive fabrication techniques, J. Synchrotron Rad. **27**, 1121 (2020).

[69] F. Seiboth, A. Kubec, A. Schropp, S. Niese, P. Gawlitza, J. Garrevoet, V. Galbierz, S. Achilles, S. Patjens, M. E. Stuckelberger *et al.*, Rapid aberration correction for diffractive x-ray optics by additive manufacturing, Opt. Express **30**, 31519 (2022).

[70] F. Berenguer, P. Godard, M. Allain, J.-M. Belloir, A. Talneau, S. Ravy, and V. Chamard, X-ray lensless microscopy from undersampled diffraction intensities, Phys. Rev. B **88**, 144101 (2013).

[71] H. Teng, P. M. Dove, and J. J. De Yoreo, Kinetics of calcite growth: Surface processes and relationships to macroscopic rate laws, Geochim. Cosmochim. Acta **64**, 2255 (2000).

[72] P. M. Dove and N. Han, Kinetics of mineral dissolution and growth as reciprocal microscopic surface processes across chemical driving force, AIP Conf. Proc. **916**, 215 (2007).

[73] P. M. Dove, N. Han, and J. J. D. Yoreo, Mechanisms of classical crystal growth theory explain quartz and silicate dissolution behavior, Proc. Natl. Acad. Sci. USA **102**, 15357 (2005).

[74] F. Mastropietro, J. Eymery, G. Carbone, S. Baudot, F. Andrieu, and V. Favre-Nicolin, Time-dependent relaxation of strained silicon-on-insulator lines using a partially coherent x-ray nanobeam, Phys. Rev. Lett. **111**, 215502 (2013).

[75] F. Lauraux, S. Yehya, S. Labat, J.-S. Micha, O. Robach, O. Kovalenko, E. Rabkin, O. Thomas, and T. W. Cornelius, In-situ force measurement during nano-indentation combined with Laue microdiffraction, Nano Select **2**, 99 (2021).

[76] J. Carnis, A. R. Kshirsagar, L. Wu, M. Dupraz, S. Labat, M. Texier, L. Favre, L. Gao, F. E. Oropeza, N. Gazit *et al.*, Twin boundary migration in an individual platinum nanocrystal during catalytic co oxidation, Nat. Commun. **12**, 5385 (2021).

[77] R. P. Millane, Multidimensional phase problems, J. Opt. Soc. Am. A **13**, 725 (1996).